Strain gradient crystal plasticity model based on generalized non-quadratic defect energy and uncoupled dissipation

Mohamed JEBAHI[a,*], Lei CAI[a], Farid ABED-MERAIM[a]

[a]*Arts et Metiers Institute of Technology, CNRS, Université de Lorraine, LEM3, F-57000 Metz, France*

Abstract

The present paper proposes a flexible Gurtin-type strain gradient crystal plasticity (SGCP) model based on generalized non-quadratic defect energy and uncoupled constitutive assumption for dissipative processes. A power-law defect energy, with adjustable order-controlling index n, is proposed to provide a comprehensive investigation into the energetic length scale effects under proportional and non-proportional loading conditions. Results of this investigation reveal quite different effects of the energetic length scale, depending on the value of n and the type of loading. For $n \geq 2$, regardless of the loading type, the energetic length scale has only influence on the rate of the classical kinematic hardening, as reported in several SGCP works. However, in the range of $n < 2$, this parameter leads to unusual nonlinear kinematic hardening effects with inflection points in the macroscopic mechanical response, resulting in an apparent increase of the yield strength under monotonic loading. More complex effects, with additional inflection points, are obtained under non-proportional loading conditions, revealing new loading history memory-like effects of the energetic length scale. Concerning dissipation, to make the dissipative effects more easily controllable, dissipative processes due to plastic strains and their gradients are assumed to be uncoupled. Separate formulations, expressed using different effective plastic strain measures, are proposed to describe such processes. Results obtained using these formulations show the great flexibility of the proposed model in controlling some major dissipative effects, such as elastic gaps. A simple way to remove these gaps under certain non-proportional loading conditions is provided. Application of the proposed uncoupled formulations to simulate the mechanical response of a sheared strip has led to accurate prediction of the plastic strain distributions, which compare very favorably with those predicted using discrete dislocation mechanics.

Keywords: Strain gradient crystal plasticity, size effects, internal length scales, non-quadratic defect energy, uncoupled dissipation

1. Introduction

In the size range between hundreds of nanometers and few tens of micrometers, the strength of materials is no longer scale-independent and the peculiar phenomenon "smaller is stronger" appears. This phenomenon has been revealed by several small scale experiments, such as micro-indentation (Ma et al., 2012; Sarac et al., 2016; Dahlberg et al., 2017), micro-bending of thin foils (Hayashi et al., 2011) and torsion of thin wires (Liu et al., 2013). Conventional plasticity theories cannot predict the size-dependent behavior of materials, due to lacking internal length scale(s). To overcome this limitation, Aifantis (1984) has proposed in a pioneering work a strain gradient plasticity (SGP) model with a single internal length scale parameter embedded in the conventional plasticity theory. This model is capable of predicting plastic deformation

Email addresses: mohamed.jebahi@ensam.eu (Mohamed JEBAHI), lei.cai@ensam.eu (Lei CAI), farid.abed-meraim@ensam.eu (Farid ABED-MERAIM)

gradients (plastic inhomogeneities), which correlate with size effects as experimentally observed and numerically predicted using dislocation mechanics (Zhou and Lesar, 2012; Dahlberg et al., 2017; Jiang et al., 2019). Plastic deformation gradients can physically be interpreted because they represent the geometrically necessary dislocations (GNDs; Ashby, 1970), which are associated with small scale crystalline incompatibilities (*e.g.,* incompatibility of the mesoscopic plastic distortion). Interesting differential-geometry-based works studying, from a geometric point of view, the kinematics of these incompatibilities and their connection with nonlocal (gradient) concepts can be found in the literature (Nye, 1953; Bilby et al., 1955; Kröner, 1958; Kondo, 1964; Lardner, 1969; Teodosiu and Sidoroff, 1976). Based on these works, Le and Stumpf (1996) and Clayton et al. (2005) have proposed generalized theoretical frameworks capable of describing the finite deformation kinematics of several classes of crystalline defects in relation with gradient plasticity theories. Thanks to their capabilities in capturing size effects, the latter theories have received a strong scientific interest since the work of Aifantis (1984). This has led to the development of a wide variety of SGP models in the last two decades. According to Hutchinson (2012), these models can be classified into two categories: (i) incremental models in which increments of higher-order stresses are related to increments of strain gradients, and (ii) non-incremental models in which the higher-order stresses themselves are expressed in terms of increments of strain gradients. Without claiming to be exhaustive, a brief review of such models is given hereafter. For more details about theoretical, numerical and experimental aspects of SGP theories, the reader is referred to the interesting review of Voyiadjis and Song (2019).

The earliest SGP models proposed in the literature belong to the category of incremental models. In this context, Mühlhaus and Alfantis (1991) have elaborated a generalized version of Aifantis (1984) model by the inclusion of higher-order spatial gradients of the equivalent plastic strain in the yield condition. In a similar way, Acharya and Bassani (2000) have proposed a simple constitutive framework in which gradient effects are incorporated in the hardening relations, using incompatibility-dependent hardening moduli. These two models preserve the classical structure of the incremental boundary value problem (with conventional stresses, equilibrium equations and boundary conditions) and are referred to in the literature as lower-order SGP models. Fleck and Hutchinson (2001) have proposed a phenomenological higher-order SGP model with the purpose of generalizing the classical J_2 flow theory to account for gradient effects at small scales. Both higher-order stresses and additional boundary conditions are considered and more than one material length scale parameters are covered in this model. However, the compatibility of such a model with the thermodynamic dissipation requirements (*i.e.*, nonnegative dissipation) has not been addressed by the authors. Gudmundson (2004) has pointed out that the nonnegative dissipation cannot always be guaranteed by this model. Later work of Gurtin and Anand (2009) has shown that this model is incompatible with thermodynamics unless the nonlocal terms are dropped. A modified version of this model in which the higher-order stresses are assumed to be fully energetic is proposed by Hutchinson (2012) to ensure its thermodynamic consistency. The assumption of no higher-order contributions to dissipation has been used in subsequent works to develop thermodynamically-acceptable incremental models (*e.g.*, Fleck et al., 2015; Nellemann et al., 2017, 2018). However, the consistency of this assumption with the current understanding of dislocation physics is questioned. Until now, there are no acceptable recipes for an incremental model including higher-order dissipative stresses (Fleck et al., 2015).

To overcome the thermodynamic deficiency of the above class of models, while considering higher-order contributions to dissipation, several authors have proposed SGP models in which the higher-order stresses are expressed in terms of increments of plastic strain gradients. These models are classified as non-incremental in the classification of Hutchinson (2012). As examples of the pioneering models in this class, one can cite the models proposed by Gurtin (2002, 2004). The great success of such a class of models has made it the class the most studied in the literature in recent years. Consequently, a large number of interesting works associated with this class have recently been published. In a series of papers, Gurtin and coworkers (Gurtin et al., 2007; Gurtin, 2008, 2010; Anand et al., 2015) have developed several variations of single- and poly-crystal SGP models, in which GNDs are represented either by scalar dislocation densities or by the full dislocation

density tensor (Nye, 1953). Mayeur and McDowell (2014) have shown that Gurtin-type models share several features with micropolar approaches (Mayeur et al., 2011). Polizzotto (2010, 2014) has numerically studied different aspects of SGP theories in small and finite deformation frameworks. Yalçinkaya et al. (2011) and Klusemann and Yalçinkaya (2013) have proposed strain gradient crystal plasticity (SGCP) models with a non-convex part in the free energy to study the plastic deformation patterning (microstructure formation) and the localization phenomena in metals. For the same purposes, finite deformation SGP models have been proposed by Anand et al. (2012); Klusemann et al. (2013) and Ling et al. (2018). In these models, the strain softening and localization are caused by the nonlinear geometric effects. Dahlberg and Faleskog (2014) have investigated the influence of the size and distribution of grains on the yield strength in poly-crystals using a SGP model and a grain boundary (GB) deformation mechanism. Wulfinghoff et al. (2015) have proposed a SGP model based on two formulations of defect energy to investigate their influence on the cyclic behavior of laminate microstructures. Bardella and Panteghini (2015) have applied a phenomenological distortion gradient plasticity model to study the effects of the plastic spin on the torsional response of thin metal wires. Bittencourt (2018) has focused on the numerical study of indentation problems using a SGCP model with two simplified hardening laws. Petryk and Stupkiewicz (2016) and Stupkiewicz and Petryk (2016) have developed and studied a novel "minimal" framework of SGCP, including a variable internal length scale derived from physically-based dislocation theory of plasticity. The effects of this "natural" length scale on several existing SGCP models have been investigated by Ryś and Petryk (2018). Based on these works, Dahlberg and Boåsen (2019) have proposed a new more general evolution equation for the length scale as a function of the plastic strains and their gradients. Compared to the class of incremental models, the present one always satisfies the thermodynamic requirements of nonnegative dissipation. However, as pointed out by several authors (*e.g.*, Hutchinson, 2012; Fleck et al., 2014, 2015), it may lead in some cases to likely unacceptable results related to finite stress variation under infinitesimal loading change.

Despite the strong scientific effort on SGP theories, several related difficulties remain to be addressed. One of them is how to define the defect energy which conditions the higher-order energetic effects. In most existing SGP models, this energy is pragmatically assumed to be quadratic in plastic strain gradients (Gurtin, 2002, 2004; Gurtin et al., 2007; Panteghini and Bardella, 2016). Using this assumption, Gurtin et al. (2007) have shown that the energetic length scale effects have only influence on the rate of the classical kinematic hardening, but not on the material strengthening. Although this statement is widely recognized when using quadratic defect energy, Bardella and Panteghini (2015) have recently shown that accounting for plastic spin in this energy can lead to strengthening effects even if quadratic form is chosen. Despite their widespread use, quadratic forms are not usual in classical dislocation theories and several investigations have shown their inadequacy in the context of SGP (*e.g.*, Cordero et al., 2010; Forest and Guéninchault, 2013). Motivated by line tension arguments, rank-one (linear) defect energy has been used by several authors (*e.g.*, Ohno and Okumura, 2007; Hurtado and Ortiz, 2013; Wulfinghoff et al., 2015). In most cases, this form shows strengthening effects of the energetic length scale. Bardella (2010) has studied the effects of the defect energy nonlinearity with quadratic and non-quadratic formulations involving plastic spin. Results by the author confirm the strengthening effects of the energetic length scale when using non-quadratic defect energy. Inspired by the statistical dislocation theory of Groma et al. (2003), Forest and Guéninchault (2013) and Wulfinghoff et al. (2015) have proposed logarithmic form of defect energy. To overcome the problem of non-smoothness and non-convexity of this form, a quadratic regularization at small dislocation densities has been used (Wulfinghoff et al., 2015; Wulfinghoff and Böhlke, 2015). El-Naaman et al. (2016) have investigated two defect energy formulations with the aim of improving the micro-structural response predicted by SGP theories. A more complete investigation of these formulations using cyclic loading, as well as an interesting discussion about the origins of the strengthening effects of the energetic length scale, have very recently been published by the authors (El-Naaman et al., 2019). In almost all existing works on the subject, the higher-order energetic effects are studied using only proportional loading. The present paper aims to corroborate these works by proposing a comprehensive investigation of these effects under both proportional

and non-proportional loading conditions. To this end, a generalized power-law defect energy formulation, with adjustable order-controlling index n, as a function of dislocation densities is proposed.

Another issue related to SGP theories is how to describe the dissipative processes. In almost all existing strain gradient works, theses processes are considered to be coupled and described with the help of generalized effective plastic strain measures, which imply plastic strains and their gradients in a coupled manner (*e.g.*, Fleck and Hutchinson, 2001; Gurtin et al., 2007; Gurtin and Anand, 2009; Hutchinson, 2012; Fleck et al., 2015; Nellemann et al., 2017, 2018). This kind of (coupled) measures makes the issue of proposing robust and flexible dissipation formulations and the control of important dissipative effects difficult. Using coupled measures, it is not easy to control, for example, the elastic gaps at initial yield or at the occurrence of non-proportional loading sources. However, in most cases, the coupling between dissipative processes in the description of dissipation is only used by assumption. The existence of such a coupling in reality appears not to be physically confirmed. Based on the current understanding of dislocation physics, there exist no physical obstacles to assuming uncoupled dissipative processes. This can be confirmed by the contributions of Forest et al. (1997, 2000) and Forest and Sievert (2003). These authors have already adopted and extensively discussed uncoupling assumptions for the description of dissipative processes associated with force-stress and couple-stress quantities in the context of Cosserat plasticity theories. The resulting uncoupled-dissipation-based models are referred to in the literature as multi-surface or multi-criterion models. In the context of phenomenological strain gradient theories, Fleck et al. (2015) have also proposed uncoupled formulations for the description of dissipative processes associated with first- and higher-order stresses. In the same context, the very recent model proposed by Panteghini et al. (2019) can also be seen as a multi-criterion model. Indeed, several independent yield surfaces are introduced to describe the higher-order dissipation, which is considered to be independent of the first-order one. With the aim of extending these works, and more particularly the work of Fleck et al. (2015), to strain gradient crystal plasticity, the present paper proposes a flexible uncoupled dissipation assumption to describe dissipative processes due to plastic slips and their gradients. These processes are assumed to be derived from a pseudo-potential that is expressed as a sum of two independent functions of plastic slips and plastic slip gradients. Conclusions about the physical consistency of this assumption will be drawn by comparing the associated results with others from the literature obtained using coupled dissipation.

Following this introduction, the present paper is organized as follows. Section 2 presents the proposed SGCP model, which is based on generalized non-quadratic defect energy and uncoupled dissipation. Section 3 discusses the implementation of a simplified two-dimensional (2D) version of the proposed model. This version is used to investigate, in a simple manner, the effects of the model constitutive parameters on the global response of a crystalline strip subjected to proportional and non-proportional shear loading conditions. Results of this investigation and discussions are presented in Section 4. Section 5 presents some concluding remarks.

2. Strain gradient crystal plasticity (SGCP) model

In this section, a Gurtin-type strain gradient crystal plasticity (SGCP) model is developed based on generalized non-quadratic defect energy and uncoupled dissipation, within the framework of small deformation.

2.1. Kinematics

Let $\mathbf{u}\left(\mathbf{x},t\right)$ denotes the displacement at time t of an arbitrary material point identified by $\mathbf{x}$ in a subregion $\mathcal{V}$ of the considered continuum. In the framework of small deformation, the displacement gradient $\boldsymbol{\nabla}\mathbf{u}$ can be additively split into elastic and plastic parts:

$$\boldsymbol{\nabla}\mathbf{u}=\mathbf{H}_e+\mathbf{H}_p \tag{1}$$

where $\mathbf{H}_e$ and $\mathbf{H}_p$ represent respectively the elastic distortion, due to stretch and rotation of the underlying lattice, and the plastic distortion, due to plastic flow. Their symmetric parts define respectively the elastic and plastic strain tensors, and their skew-symmetric parts give respectively the elastic and plastic rotation tensors:

$$\boldsymbol{\varepsilon}_e = \frac{1}{2}\left[\mathbf{H}_e + \mathbf{H}_e^T\right],\ \boldsymbol{\varepsilon}_p = \frac{1}{2}\left[\mathbf{H}_p + \mathbf{H}_p^T\right],\ \boldsymbol{\omega}_e = \frac{1}{2}\left[\mathbf{H}_e - \mathbf{H}_e^T\right],\ \boldsymbol{\omega}_p = \frac{1}{2}\left[\mathbf{H}_p - \mathbf{H}_p^T\right] \tag{2}$$

In single-crystal plasticity framework, it is widely acknowledged that plastic flow occurs through slip on prescribed slip systems, with each system α defined by a slip direction $\mathbf{s}^\alpha$ and a slip-plane normal $\mathbf{m}^\alpha$ unit vectors. With this description of plastic flow, the rate of $\mathbf{H}_p$ can be expressed as:

$$\dot{\mathbf{H}}_p = \sum_{\alpha=1}^{q} \dot{\gamma}^\alpha \left[\mathbf{s}^\alpha \otimes \mathbf{m}^\alpha\right] \tag{3}$$

where $\dot{\gamma}^\alpha$ is the rate of plastic slip on slip system α, q is the total number of slip systems, and "$\otimes$" is the tensor product operator. Using this expression, the plastic strain rate tensor $\dot{\boldsymbol{\varepsilon}}_p$ can be written as:

$$\dot{\boldsymbol{\varepsilon}}_p = \sum_{\alpha=1}^{q} \dot{\gamma}^\alpha \mathbf{P}^\alpha \tag{4}$$

where $\mathbf{P}^\alpha$ is the symmetrized Schmid tensor associated with slip system α :

$$\mathbf{P}^\alpha = \frac{1}{2}\left(\mathbf{s}^\alpha \otimes \mathbf{m}^\alpha + \mathbf{m}^\alpha \otimes \mathbf{s}^\alpha\right) \tag{5}$$

Equation (3), together with (1) and (2), can also be used to obtain a relation between $\dot{\mathbf{u}}$, $\dot{\boldsymbol{\varepsilon}}_e$, $\dot{\boldsymbol{\omega}}_e$ and $\dot{\gamma}^\alpha$:

$$\boldsymbol{\nabla}\dot{\mathbf{u}} = \dot{\boldsymbol{\varepsilon}}_e + \dot{\boldsymbol{\omega}}_e + \sum_{\alpha=1}^{q} \dot{\gamma}^\alpha \mathbf{s}^\alpha \otimes \mathbf{m}^\alpha \tag{6}$$

In what follows, $\boldsymbol{\gamma}$ and $\dot{\boldsymbol{\gamma}}$ (in bold) will be used to designate the list of plastic slips and their rates, respectively:

$$\boldsymbol{\gamma} = \left(\gamma^1, \gamma^2, ..., \gamma^q\right), \quad \dot{\boldsymbol{\gamma}} = \left(\dot{\gamma}^1, \dot{\gamma}^2, ..., \dot{\gamma}^q\right) \tag{7}$$

2.2. Balance equations

The balance equations of the proposed strain gradient crystal plasticity (SGCP) model will be derived based on a generalization of the virtual power density of internal forces. In the present enhanced continuum, both displacement and plastic slip fields are considered as primary and controllable variables. As a consequence, the rates of these variables and their gradients will be involved in the definition of the virtual power density of internal forces:

$$\left\{\dot{\mathbf{u}},\ \boldsymbol{\nabla}\dot{\mathbf{u}},\ \dot{\boldsymbol{\gamma}},\ \boldsymbol{\nabla}\dot{\boldsymbol{\gamma}}\right\} \tag{8}$$

The internal virtual power expended within a subregion $\mathcal{V}$ of the considered continuum is computed by means of density p_{int} that is assumed to depend linearly on all the virtual variations of the modeling variables given by (8):

$$p_{int} = \mathbf{f}_i \cdot \delta\dot{\mathbf{u}} + \boldsymbol{\sigma} : \delta\boldsymbol{\nabla}\dot{\mathbf{u}} + \sum_{\alpha=1}^{q} \kappa^\alpha\, \delta\dot{\gamma}^\alpha + \sum_{\alpha=1}^{q} \boldsymbol{\xi}^\alpha \cdot \delta\boldsymbol{\nabla}\dot{\gamma}^\alpha \tag{9}$$

where $\mathbf{f}_i$ is internal volumetric force, $\boldsymbol{\sigma}$ is macroscopic stress tensor, κ^α and $\boldsymbol{\xi}^\alpha$ are respectively microscopic stress scalar (work-conjugate to γ^α) and microscopic stress vector (work-conjugate to $\boldsymbol{\nabla}\gamma^\alpha$) associated with slip system α, and ": " is the double-dot product operator. The introduced microscopic stress scalar and vector are referred to hereafter as first- and higher-order microscopic stresses, respectively. Since the virtual power density of internal forces must be objective (*i.e.*, independent of the frame in which the virtual variations are expressed), $\mathbf{f}_i$ must be zero and $\boldsymbol{\sigma}$ must be symmetric. By using (6), it is then easy to demonstrate that:

$$p_{int} = \boldsymbol{\sigma} : \delta\dot{\boldsymbol{\varepsilon}}_e + \sum_{\alpha=1}^{q} \left(\kappa^\alpha + \tau^\alpha\right) \delta\dot{\gamma}^\alpha + \sum_{\alpha=1}^{q} \boldsymbol{\xi}^\alpha \cdot \delta\boldsymbol{\nabla}\dot{\gamma}^\alpha \tag{10}$$

where τ^α is resolved shear stress on slip system α defined by $\tau^\alpha = \boldsymbol{\sigma} : (\mathbf{s}^\alpha \otimes \mathbf{m}^\alpha)$. Introducing a new first-order microscopic stress scalar π^α such that $\pi^\alpha = \kappa^\alpha + \tau^\alpha$, a more compact form of p_{int}, which is similar to that used by Gurtin et al. (2007), can be obtained:

$$p_{int} = \boldsymbol{\sigma} : \delta\dot{\boldsymbol{\varepsilon}}_e + \sum_{\alpha=1}^{q} \pi^\alpha \, \delta\dot{\gamma}^\alpha + \sum_{\alpha=1}^{q} \boldsymbol{\xi}^\alpha \cdot \delta\boldsymbol{\nabla}\dot{\gamma}^\alpha \tag{11}$$

Considering this expression of p_{int}, the internal virtual power expended within the subregion $\mathcal{V}$ can be expressed as follows:

$$\mathcal{P}_{int} = \int_{\mathcal{V}} \boldsymbol{\sigma} : \delta\dot{\boldsymbol{\varepsilon}}_e \, dv + \sum_{\alpha=1}^{q} \int_{\mathcal{V}} \pi^\alpha \, \delta\dot{\gamma}^\alpha \, dv + \sum_{\alpha=1}^{q} \int_{\mathcal{V}} \boldsymbol{\xi}^\alpha \cdot \delta\boldsymbol{\nabla}\dot{\gamma}^\alpha \, dv \tag{12}$$

Assuming that no external body forces act on the subregion $\mathcal{V}$ and the contact forces acting on its boundary $\mathcal{S}$ can be represented by a macroscopic traction vector $\mathbf{t}$ and a microscopic traction scalar χ^α on each slip system α, the external virtual power expended on $\mathcal{V}$ can be expressed as:

$$\mathcal{P}_{ext} = \int_{\mathcal{S}} \mathbf{t} \cdot \delta\dot{\mathbf{u}} \, ds + \sum_{\alpha=1}^{q} \int_{\mathcal{S}} \chi^\alpha \, \delta\dot{\gamma}^\alpha \, ds \tag{13}$$

Application of the virtual power principle, which postulates that the internal and external virtual powers are balanced for any subregion $\mathcal{V}$ and virtual variations of the modeling variables, leads to two kinds of balance equations (since two kinds of primary variables are used). Macroscopic balance equations can be obtained by setting:

$$\delta\dot{\boldsymbol{\gamma}} = \mathbf{0} \quad (i.e., \ \delta\boldsymbol{\nabla}\dot{\mathbf{u}} = \delta\dot{\boldsymbol{\varepsilon}}_e + \delta\dot{\boldsymbol{\omega}}_e) \tag{14}$$

Considering the symmetry of the stress tensor $\boldsymbol{\sigma}$, after application of the Gauss (divergence) theorem, the virtual power balance becomes:

$$\int_{\mathcal{V}} (\boldsymbol{\nabla} \cdot \boldsymbol{\sigma}) \cdot \delta\dot{\mathbf{u}} \, dv = \int_{\mathcal{S}} (\boldsymbol{\sigma} \cdot \mathbf{n} - \mathbf{t}) \cdot \delta\dot{\mathbf{u}} \, ds \tag{15}$$

which is valid for any arbitrary subregion $\mathcal{V}$ and virtual variations of the modeling variables. This leads to the classical balance equations (static case) and the well-known traction conditions:

$$\begin{cases} \boldsymbol{\nabla} \cdot \boldsymbol{\sigma} = \mathbf{0} & \text{in} \quad \mathcal{V} \\ \boldsymbol{\sigma} \cdot \mathbf{n} = \mathbf{t} & \text{on} \quad \mathcal{S} \end{cases} \tag{16}$$

with $\mathbf{n}$ the outward unit normal to $\mathcal{S}$. The microscopic counterparts of these balance equations and boundary conditions can be obtained by setting:

$$\delta\dot{\mathbf{u}} = \mathbf{0} \quad (i.e.,\ \delta\dot{\boldsymbol{\varepsilon}}_e + \delta\dot{\boldsymbol{\omega}}_e = -\sum_{\alpha=1}^{q} \delta\dot{\gamma}^\alpha \mathbf{s}^\alpha \otimes \mathbf{m}^\alpha) \tag{17}$$

Considering (17), it can be demonstrated that:

$$\boldsymbol{\sigma} : \delta\dot{\boldsymbol{\varepsilon}}_e = -\sum_{\alpha=1}^{q} \tau^\alpha\, \delta\dot{\gamma}^\alpha \tag{18}$$

which leads, after application of the Gauss theorem, to the following form of the virtual power balance:

$$\sum_{\alpha=1}^{q} \int_{\mathcal{V}} \left(\tau^\alpha + \boldsymbol{\nabla}\cdot\boldsymbol{\xi}^\alpha - \pi^\alpha\right)\, \delta\dot{\gamma}^\alpha\, dv = \sum_{\alpha=1}^{q} \int_{\mathcal{S}} \left(\boldsymbol{\xi}^\alpha \cdot \mathbf{n} - \chi^\alpha\right)\, \delta\dot{\gamma}^\alpha\, ds = 0 \tag{19}$$

Since (19) is valid for any arbitrary subregion $\mathcal{V}$ and virtual variations of the modeling variables, the microscopic balance equation (static case) and the microscopic traction condition on each slip system α can be obtained:

$$\left\{ \begin{array}{rcll} \tau^\alpha + \boldsymbol{\nabla}\cdot\boldsymbol{\xi}^\alpha - \pi^\alpha & = & 0 & \text{in} \quad \mathcal{V} \\ \boldsymbol{\xi}^\alpha \cdot \mathbf{n} & = & \chi^\alpha & \text{on} \quad \mathcal{S} \end{array} \right. \tag{20}$$

2.3. Dissipation inequality

The dissipation inequality in local form will be derived based on the second law of thermodynamics. In a mechanical perspective, this law can be expressed as follows: the temporal increase in free energy of any subregion $\mathcal{V}$ is less than or equal to the external power expended on this subregion. Mathematically, this means:

$$\dot{\overline{\int_{\mathcal{V}} \psi\, dv}} \leq \mathcal{P}_{ext} \tag{21}$$

where ψ is free energy per unit volume, which is assumed to be controlled by the following set of state variables: $\{\boldsymbol{\varepsilon}_e,\ \boldsymbol{\gamma},\ \boldsymbol{\nabla\gamma}\}$, as usually done in the framework of strain gradient crystal plasticity.

$$\psi = \psi\left(\boldsymbol{\varepsilon}_e,\ \boldsymbol{\gamma},\ \boldsymbol{\nabla\gamma}\right) \tag{22}$$

Considering the identity $\mathcal{P}_{int} = \mathcal{P}_{ext}$, the above inequality can be rewritten in terms of internal power components as follows:

$$\int_{\mathcal{V}} \left(\dot{\psi} - \boldsymbol{\sigma} : \dot{\boldsymbol{\varepsilon}}_e - \sum_{\alpha=1}^{q} \pi^\alpha\, \dot{\gamma}^\alpha - \sum_{\alpha=1}^{q} \boldsymbol{\xi}^\alpha \cdot \boldsymbol{\nabla}\dot{\gamma}^\alpha \right)\, dv \leq 0 \tag{23}$$

with

$$\dot{\psi}\left(\boldsymbol{\varepsilon}_e,\ \boldsymbol{\gamma},\ \boldsymbol{\nabla\gamma}\right) = \frac{\partial\psi}{\partial\boldsymbol{\varepsilon}_e} : \dot{\boldsymbol{\varepsilon}}_e + \sum_{\alpha=1}^{q} \frac{\partial\psi}{\partial\gamma^\alpha}\, \dot{\gamma}^\alpha + \sum_{\alpha=1}^{q} \frac{\partial\psi}{\partial\boldsymbol{\nabla}\gamma^\alpha} \cdot \boldsymbol{\nabla}\dot{\gamma}^\alpha \tag{24}$$

Since $\mathcal{V}$ is arbitrary, (23) yields the local dissipation inequality (also called local free energy imbalance):

$$\mathcal{D} = \boldsymbol{\sigma} : \dot{\boldsymbol{\varepsilon}}_e + \sum_{\alpha=1}^{q} \pi^\alpha \, \dot{\gamma}^\alpha + \sum_{\alpha=1}^{q} \boldsymbol{\xi}^\alpha \cdot \boldsymbol{\nabla} \dot{\gamma}^\alpha - \dot{\psi} \geq 0 \tag{25}$$

Replacing $\dot{\psi}$ by its expression (24), this local inequality can be rewritten as follows:

$$\mathcal{D} = \left(\boldsymbol{\sigma} - \frac{\partial \psi}{\partial \boldsymbol{\varepsilon}_e} \right) : \dot{\boldsymbol{\varepsilon}}_e + \sum_{\alpha=1}^{q} \left(\pi^\alpha - \frac{\partial \psi}{\partial \gamma^\alpha} \right) \dot{\gamma}^\alpha + \sum_{\alpha=1}^{q} \left(\boldsymbol{\xi}^\alpha - \frac{\partial \psi}{\partial \boldsymbol{\nabla} \gamma^\alpha} \right) \cdot \boldsymbol{\nabla} \dot{\gamma}^\alpha \geq 0. \tag{26}$$

In the present SGCP model, the macroscopic stress $\boldsymbol{\sigma}$ is regarded as energetic quantity having no contribution to dissipation:

$$\boldsymbol{\sigma} = \frac{\partial \psi}{\partial \boldsymbol{\varepsilon}_e} \tag{27}$$

whereas the microscopic stresses π^α and $\boldsymbol{\xi}^\alpha$ on each slip system α may possibly be divided into energetic and dissipative parts:

$$\pi^\alpha = \pi^\alpha_{en} + \pi^\alpha_{dis}, \qquad \boldsymbol{\xi}^\alpha = \boldsymbol{\xi}^\alpha_{en} + \boldsymbol{\xi}^\alpha_{dis} \tag{28}$$

with

$$\pi^\alpha_{en} = \frac{\partial \psi}{\partial \gamma^\alpha}, \qquad \boldsymbol{\xi}^\alpha_{en} = \frac{\partial \psi}{\partial \boldsymbol{\nabla} \gamma^\alpha} \tag{29}$$

Therefore, the local dissipation inequality can be simplified as follows:

$$\mathcal{D} = \sum_{\alpha=1}^{q} \pi^\alpha_{dis} \, \dot{\gamma}^\alpha + \sum_{\alpha=1}^{q} \boldsymbol{\xi}^\alpha_{dis} \cdot \boldsymbol{\nabla} \dot{\gamma}^\alpha \geq 0 \tag{30}$$

This inequality will be considered in the definition of suitable constitutive laws for the dissipative microscopic stresses π^α_{dis} and $\boldsymbol{\xi}^\alpha_{dis}$ on each slip system α.

2.4. Constitutive laws

Constitutive relations are derived in this subsection to describe the evolution of the macroscopic and microscopic stresses involved in the balance equations (first lines of systems (16) and (20)), and then to reproduce the mechanical behavior of the considered continuum. This behavior is assumed to be governed by energetic and dissipative processes.

2.4.1. Energetic constitutive laws

The energetic processes are represented by the density of free energy ψ. In this work, the classical decomposition of ψ into an elastic strain energy ψ_e and a defect energy ψ_p is adopted. ψ_e is assumed to be a quadratic function of $\boldsymbol{\varepsilon}_e$:

$$\psi_e \left(\boldsymbol{\varepsilon}_e \right) = \frac{1}{2} \, \boldsymbol{\varepsilon}_e : \mathbf{C} : \boldsymbol{\varepsilon}_e \tag{31}$$

where $\mathbf{C}$ is the elasticity tensor, which is assumed to be symmetric and positive-definite. Building on the work of Gurtin et al. (2007), ψ_p is assumed to be function of dislocation densities:

$$\boldsymbol{\rho} = \left(\rho_{\vdash}^{1},\, \rho_{\vdash}^{2},\, ...,\, \rho_{\vdash}^{q},\, \rho_{\odot}^{1},\, \rho_{\odot}^{2},\, ...,\, \rho_{\odot}^{q}\right) \tag{32}$$

where $\rho_{\vdash}^{\alpha}$ and $\rho_{\odot}^{\alpha}$ denote respectively edge and screw dislocation densities on slip system α. As shown by Arsenlis and Parks (1999), these quantities can be calculated by:

$$\rho_{\vdash}^{\alpha} = -\mathbf{s}^{\alpha} \cdot \boldsymbol{\nabla}\gamma^{\alpha}, \qquad \rho_{\odot}^{\alpha} = \mathbf{l}^{\alpha} \cdot \boldsymbol{\nabla}\gamma^{\alpha} \tag{33}$$

where $\mathbf{l}^{\alpha}$ is the line direction of dislocation distribution defined by $\mathbf{l}^{\alpha} = \mathbf{m}^{\alpha} \times \mathbf{s}^{\alpha}$ ("$\times$" is cross product operator). However, contrary to the work of Gurtin et al. (2007), in the present paper, ψ_p is assumed to be non-quadratic in these densities. A power-law form, with adjustable order-controlling index n, is applied to define this energy:

$$\psi_p\left(\boldsymbol{\rho}\right) = \frac{1}{n}\, X_0\, l_{en}^{n} \sum_{\alpha=1}^{q} \left[\left|\rho_{\vdash}^{\alpha}\right|^{n} + \left|\rho_{\odot}^{\alpha}\right|^{n}\right] \tag{34}$$

where X_0 is a constant representing the energetic slip resistance, and l_{en} is an energetic length scale. To ensure the convexity of ψ_p, the defect energy index n must be greater than or equal to 1 ($n \geq 1$). Using (31) and (34), the free energy density can be expressed as:

$$\psi\left(\boldsymbol{\varepsilon}_e, \boldsymbol{\rho}\right) = \frac{1}{2}\, \boldsymbol{\varepsilon}_e : \mathbf{C} : \boldsymbol{\varepsilon}_e + \frac{1}{n}\, X_0\, l_{en}^{n} \sum_{\alpha=1}^{q} \left[\left|\rho_{\vdash}^{\alpha}\right|^{n} + \left|\rho_{\odot}^{\alpha}\right|^{n}\right] \tag{35}$$

The partial derivatives of this expression with respect to the state variables presented in (22) provide the energetic constitutive laws that describe the evolution of the energetic stresses involved in the balance equations (first lines of systems (16) and (20)). The (energetic) macroscopic stress tensor $\boldsymbol{\sigma}$ can be expressed as:

$$\boldsymbol{\sigma} = \frac{\partial \psi}{\partial \boldsymbol{\varepsilon}_e} = \mathbf{C} : \boldsymbol{\varepsilon}_e \tag{36}$$

Since there is no explicit dependence between the assumed form of ψ and $\boldsymbol{\gamma}$, the energetic part of the microscopic stress scalar π_{en}^{α} is zero for any slip system α:

$$\pi_{en}^{\alpha} = \frac{\partial \psi}{\partial \gamma^{\alpha}} = 0 \tag{37}$$

The energetic microscopic stress vector $\boldsymbol{\xi}_{en}^{\alpha}$ on slip system α can be expressed as:

$$\boldsymbol{\xi}_{en}^{\alpha} = \frac{\partial \psi\left(\boldsymbol{\varepsilon}_e, \boldsymbol{\rho}\right)}{\partial \boldsymbol{\nabla}\gamma^{\alpha}} = X_0\, l_{en}^{n} \left[\left|\mathbf{s}^{\alpha} \cdot \boldsymbol{\nabla}\gamma^{\alpha}\right|^{n-2}\, \mathbf{s}^{\alpha} \otimes \mathbf{s}^{\alpha} + \left|\mathbf{l}^{\alpha} \cdot \boldsymbol{\nabla}\gamma^{\alpha}\right|^{n-2}\, \mathbf{l}^{\alpha} \otimes \mathbf{l}^{\alpha}\right] \cdot \boldsymbol{\nabla}\gamma^{\alpha} \tag{38}$$

2.4.2. Dissipative constitutive laws

As discussed in the introduction, in almost all existing strain gradient theories involving both first- and higher-order dissipative microscopic stresses, the evolution of the latter is described using constitutive equations based on generalized effective plastic strain measures, which imply plastic strains and their gradients in a coupled manner (*e.g.*, Fleck and Hutchinson, 2001; Gurtin et al., 2007; Gurtin and Anand, 2009; Hutchinson, 2012; Fleck et al., 2015; Nellemann et al., 2017, 2018). An example of these measures is:

$$\dot{E}_p = \sqrt{\left\|\dot{\boldsymbol{\varepsilon}}_p\right\|^2 + l_{dis}^2\, \left\|\boldsymbol{\nabla}\dot{\boldsymbol{\varepsilon}}_p\right\|^2}, \qquad E_p = \int \dot{E}_p dt \tag{39}$$

where l_{dis} is a dissipative length scale. However, the use of such coupled measures to define the dissipative constitutive equations largely restricts their flexibility and makes the control of some numerically noticed unusual behaviors, *e.g.*, the elastic gap at initial yield (Hutchinson, 2012; Fleck et al., 2015), difficult. Actually, in most cases, these coupled measures are only used by assumption, as the coupling between first- and higher-order dissipative processes is hitherto not physically confirmed.

To allow for more flexible control of major dissipative effects, in present work, the dissipative microscopic stresses are derived from a dissipation functional φ, which is postulated based on the assumption of uncoupled dissipative contributions from plastic slips and plastic slip gradients. In spirit of multi-criterion approaches available in the literature (Forest et al., 1997, 2000; Forest and Sievert, 2003; Fleck et al., 2015; Panteghini et al., 2019), this functional is assumed to be divided into two independent parts: one part, which describes first-order dissipative effects, is only function of plastic slips and their rates φ_π; and the other part, which describes higher-order dissipative effects, depends only on gradients of plastic slips and their rates φ_ξ. Note that similar (uncoupling) assumption was applied in the recent contribution of Fleck et al. (2015) to describe first- and higher-order dissipative effects in the context of phenomenological strain gradient plasticity. Therefore, the present work can be seen as an extension of this contribution to strain gradient crystal plasticity.

Define independent first- and higher-order effective plastic strains for each slip system α (e_π^α and e_ξ^α, respectively) as follows:

$$\dot{e}_\pi^\alpha = |\dot{\gamma}^\alpha| = \sqrt{(\dot{\gamma}^\alpha)^2}, \qquad e_\pi^\alpha = \int \dot{e}_\pi^\alpha \, dt \tag{40}$$

$$\dot{e}_\xi^\alpha = \| l_{dis} \, \boldsymbol{\nabla}^\alpha \dot{\gamma}^\alpha \| = l_{dis} \sqrt{(\boldsymbol{\nabla}^\alpha \dot{\gamma}^\alpha)^2}, \qquad e_\xi^\alpha = \int \dot{e}_\xi^\alpha \, dt \tag{41}$$

where $\boldsymbol{\nabla}^\alpha$ is the projection of $\boldsymbol{\nabla}$ onto slip system α:

$$\boldsymbol{\nabla}^\alpha \phi = (\mathbf{s}^\alpha \cdot \boldsymbol{\nabla}\phi) \, \mathbf{s}^\alpha + (\mathbf{l}^\alpha \cdot \boldsymbol{\nabla}\phi) \, \mathbf{l}^\alpha \tag{42}$$

The proposed uncoupled dissipation functional can be expressed as:

$$\varphi \left(\dot{\mathbf{e}}_\pi, \, \mathbf{e}_\pi, \, \dot{\mathbf{e}}_\xi, \, \mathbf{e}_\xi \right) \quad = \quad \varphi_\pi \left(\dot{\mathbf{e}}_\pi, \, \mathbf{e}_\pi \right) + \varphi_\xi \left(\dot{\mathbf{e}}_\xi, \, \mathbf{e}_\xi \right) \tag{43}$$

with

$$\dot{\mathbf{e}}_\pi = \left(\dot{e}_\pi^1, \, \dot{e}_\pi^2, \, ..., \dot{e}_\pi^q \right), \; \mathbf{e}_\pi = \left(e_\pi^1, \, e_\pi^2, \, ..., e_\pi^q \right), \; \dot{\mathbf{e}}_\xi = \left(\dot{e}_\xi^1, \, \dot{e}_\xi^2, \, ..., \dot{e}_\xi^q \right), \; \mathbf{e}_\xi = \left(e_\xi^1, \, e_\xi^2, \, ..., e_\xi^q \right) \tag{44}$$

For comparison purposes, expressions of φ_π and φ_ξ are postulated in such a way as to obtain dissipative microscopic stresses having forms close to those proposed by Gurtin et al. (2007):

$$\varphi_i \left(\dot{\mathbf{e}}_i, \, \mathbf{e}_i \right) = \sum_{\alpha=1}^{q} S_i^\alpha \, \frac{\dot{\gamma}_0^\alpha}{m+1} \left[\frac{\dot{e}_i^\alpha}{\dot{\gamma}_0^\alpha} \right]^{m+1} \tag{45}$$

where the subscript i takes as value π or ξ in reference to first- or higher-order dissipative microscopic stresses, $\dot{\gamma}_0^\alpha > 0$ is a constant strain rate representative of the flow rates of interest, $m > 0$ is a constant characterizing the rate-sensitivity of the considered material, and S_i^α ($i \in \{\pi, \, \xi\}$) are stress-dimensional internal state variables ($S_\pi^\alpha > 0$ and $S_\xi^\alpha \geq 0$). These variables are referred to hereafter as dissipative slip resistances and their evolutions are assumed to be governed by:

$$\dot{S}_i^\alpha = \sum_{\beta=1}^{q} h_i^{\alpha\beta} \left(S_i^\beta \right) \dot{e}_i^\beta \quad \text{with} \quad S_i^\alpha \left(0 \right) = S_{i0} \tag{46}$$

S_{i0} ($i \in \{\pi,\, \xi\}$) are initial dissipative slip resistances (with $S_{\pi 0} > 0$ and $S_{\xi 0} \geq 0$), and $h_i^{\alpha\beta}$ ($i \in \{\pi,\, \xi\}$) are positive hardening moduli assumed to evolve according to:

$$h_i^{\alpha\beta}\left(S_i^{\beta}\right) = \underbrace{s^{\alpha\beta}\, h_i\left(S_i^{\beta}\right)}_{\text{Self hardening}} + \underbrace{l^{\alpha\beta}\, h_i\left(S_i^{\beta}\right)}_{\text{Latent hardening}} \tag{47}$$

$s^{\alpha\beta}$ is self hardening parameter marking coplanar slip planes and is defined by:

$$s^{\alpha\beta} = \begin{cases} 1 & \text{if } \mathbf{m}^{\alpha} \wedge \mathbf{m}^{\beta} = \mathbf{0} \\ 0 & \text{otherwise} \end{cases} \tag{48}$$

and $l^{\alpha\beta}$ is latent hardening parameter defined in this work as:

$$l^{\alpha\beta} = \left|\mathbf{s}^{\alpha} \cdot \mathbf{s}^{\beta}\right| \left\|\mathbf{m}^{\alpha} \wedge \mathbf{m}^{\beta}\right\| \tag{49}$$

to take into account the influence of the relative misorientation of slip planes on the hardening moduli. h_i ($i \in \{\pi,\, \xi\}$) are self-hardening functions which, motivated by several works from the literature (*e.g.*, Kalidindi et al., 1992; Gurtin et al., 2007), are assumed to be defined as:

$$h_i\left(S_i^{\beta}\right) = \begin{cases} H_i \left(1 - \frac{S_i^{\beta}}{S_{iF}}\right)^a & \text{for} \quad S_{i0} \leq S_i^{\beta} < S_{iF} \\ 0 & \text{for} \quad S_i^{\beta} \geq S_{iF} \end{cases} \tag{50}$$

with $S_{iF} > S_{i0}$, $a \geq 1$ and $H_i \geq 0$.

Based on the above definitions of the ingredients of the proposed dissipation functional φ, it can easily be verified that this functional is nonnegative and convex in $\dot{\gamma}^{\alpha}$ and $\boldsymbol{\nabla}\dot{\gamma}^{\alpha}$, which guarantees a priori satisfaction of the second principle of thermodynamics (nonnegative dissipation). The partial derivatives of φ with respect to $\dot{\gamma}^{\alpha}$ and $\boldsymbol{\nabla}\dot{\gamma}^{\alpha}$ give the expressions of the dissipative stress scalar π_{dis}^{α} and vector $\boldsymbol{\xi}_{dis}^{\alpha}$ on slip system α:

$$\pi_{dis}^{\alpha} = \frac{\partial \varphi}{\partial \dot{\gamma}^{\alpha}} = S_{\pi}^{\alpha} \left[\frac{\dot{e}_{\pi}^{\alpha}}{\dot{\gamma}_0^{\alpha}}\right]^m \frac{\dot{\gamma}^{\alpha}}{\dot{e}_{\pi}^{\alpha}} \tag{51}$$

$$\boldsymbol{\xi}_{dis}^{\alpha} = \frac{\partial \varphi}{\partial \boldsymbol{\nabla}\dot{\gamma}^{\alpha}} = S_{\xi}^{\alpha}\, l_{dis}^2 \left[\frac{\dot{e}_{\xi}^{\alpha}}{\dot{\gamma}_0^{\alpha}}\right]^m \frac{\boldsymbol{\nabla}^{\alpha}\dot{\gamma}^{\alpha}}{\dot{e}_{\xi}^{\alpha}} \tag{52}$$

As mentioned above, the dissipation functional proposed in this work φ leads to dissipative microscopic stresses close to those postulated by Gurtin et al. (2007) based on the normality rule. The latter can be obtained from (51) and (52) by replacing the first- and higher-order effective plastic strains by a coupled one defined by:

$$\dot{d}^{\alpha} = \sqrt{\left(\dot{e}_{\pi}^{\alpha}\right)^2 + \left(\dot{e}_{\xi}^{\alpha}\right)^2}, \qquad d^{\alpha} = \int \dot{d}^{\alpha}\, dt \tag{53}$$

and by replacing S_{π}^{α} and S_{ξ}^{α} by a single strictly positive slip resistance S^{α} calculated based on $\dot{d}^{\alpha}$.

2.5. Flow rules

Based on the expressions of the microscopic stresses, the microscopic balance equation associated with slip system α (first line of system (20)) can be reformulated as follows:

$$\tau^{\alpha} + \boldsymbol{\nabla} \cdot \boldsymbol{\xi}^{\alpha}_{en} + \boldsymbol{\nabla} \cdot \boldsymbol{\xi}^{\alpha}_{dis} - \pi^{\alpha}_{dis} = 0 \tag{54}$$

When augmented by the microscopic constitutive laws (38), (51) and (52), this equation acts as a flow rule associated with slip system α:

$$\tau^{\alpha} + \boldsymbol{\nabla} \cdot \boldsymbol{\xi}^{\alpha}_{en} + \boldsymbol{\nabla} \cdot \left\{ S^{\alpha}_{\xi}\, l^{2}_{dis} \left[\frac{\dot{e}^{\alpha}_{\xi}}{\dot{\gamma}^{\alpha}_{0}} \right]^{m} \frac{\boldsymbol{\nabla}^{\alpha} \dot{\gamma}^{\alpha}}{\dot{e}^{\alpha}_{\xi}} \right\} - S^{\alpha}_{\pi} \left[\frac{\dot{e}^{\alpha}_{\pi}}{\dot{\gamma}^{\alpha}_{0}} \right]^{m} \frac{\dot{\gamma}^{\alpha}}{\dot{e}^{\alpha}_{\pi}} = 0 \tag{55}$$

Bearing in mind (38), $\boldsymbol{\nabla} \cdot \boldsymbol{\xi}^{\alpha}_{en}$ can be expressed as:

$$\boldsymbol{\nabla} \cdot \boldsymbol{\xi}^{\alpha}_{en} \;\; = \;\; \mathbf{A}^{\alpha\alpha} : \boldsymbol{\nabla}\boldsymbol{\nabla}\gamma^{\alpha} \tag{56}$$

with

$$\mathbf{A}^{\alpha\alpha} = (n-1)\; X_0\, l^{n}_{en} \left[\left| \mathbf{s}^{\alpha} \cdot \boldsymbol{\nabla}\gamma^{\alpha} \right|^{n-2} \mathbf{s}^{\alpha} \otimes \mathbf{s}^{\alpha} + \left| \mathbf{l}^{\alpha} \cdot \boldsymbol{\nabla}\gamma^{\alpha} \right|^{n-2} \mathbf{l}^{\alpha} \otimes \mathbf{l}^{\alpha} \right] \tag{57}$$

Using (56), the flow rule (55) becomes:

$$\tau^{\alpha} + \mathbf{A}^{\alpha\alpha} : \boldsymbol{\nabla}\boldsymbol{\nabla}\gamma^{\alpha} + \boldsymbol{\nabla} \cdot \left\{ S^{\alpha}_{\xi}\, l^{2}_{dis} \left[\frac{\dot{e}^{\alpha}_{\xi}}{\dot{\gamma}^{\alpha}_{0}} \right]^{m} \frac{\boldsymbol{\nabla}^{\alpha} \dot{\gamma}^{\alpha}}{\dot{e}^{\alpha}_{\xi}} \right\} - S^{\alpha}_{\pi} \left[\frac{\dot{e}^{\alpha}_{\pi}}{\dot{\gamma}^{\alpha}_{0}} \right]^{m} \frac{\dot{\gamma}^{\alpha}}{\dot{e}^{\alpha}_{\pi}} = 0. \tag{58}$$

The second term in the above equation, being energetic, represents the negative of a backstress, leading to Bauschinger effects in the flow rule. The last two terms of this equation are dissipative (resulting from the dissipation functional). A reversal of the flow direction ($\dot{\gamma}^{\alpha} \rightarrow -\dot{\gamma}^{\alpha}$) simply changes their sign. Therefore, these terms represent the dissipative (isotropic) hardening. The flow rule (58) can then be written in a more convenient form as:

$$\tau^{\alpha} \;\; - \;\; \underbrace{\left(-\mathbf{A}^{\alpha\alpha} : \boldsymbol{\nabla}\boldsymbol{\nabla}\gamma^{\alpha} \right)}_{\text{Energetic backstress}} \;\; = \;\; \underbrace{S^{\alpha}_{\pi} \left[\frac{\dot{e}^{\alpha}_{\pi}}{\dot{\gamma}^{\alpha}_{0}} \right]^{m} \frac{\dot{\gamma}^{\alpha}}{\dot{e}^{\alpha}_{\pi}} - \boldsymbol{\nabla} \cdot \left\{ S^{\alpha}_{\xi}\, l^{2}_{dis} \left[\frac{\dot{e}^{\alpha}_{\xi}}{\dot{\gamma}^{\alpha}_{0}} \right]^{m} \frac{\boldsymbol{\nabla}^{\alpha} \dot{\gamma}^{\alpha}}{\dot{e}^{\alpha}_{\xi}} \right\}}_{\text{Dissipative hardening}} \tag{59}$$

3. Simplified two-dimensional version of the SGCP model and numerical implementation

In this section, a simplified two-dimensional (2D) version of the proposed SGCP model is derived and implemented to investigate, in a simple manner, the influence of the constitutive parameters and the uncoupled dissipation functional on the global response of the considered continuum.

3.1. Simplified 2D SGCP model

The plane strain condition is adopted for the 2D model. Under this condition, the displacement field can be degenerated as:

$$\mathbf{u}\left(\mathbf{x}, t\right) = u_1\left(x_1, x_2, t\right)\, \mathbf{e}_1 + u_2\left(x_1, x_2, t\right)\, \mathbf{e}_2 \tag{60}$$

which results in a displacement gradient $\boldsymbol{\nabla}\mathbf{u}$ that is independent of x_3. Furthermore, attention is restricted to planar slip systems, *i.e.*, slip systems satisfying:

$$\mathbf{s}^{\alpha} \cdot \mathbf{e}_3 = 0, \;\; \mathbf{m}^{\alpha} \cdot \mathbf{e}_3 = 0, \;\; \mathbf{s}^{\alpha} \times \mathbf{m}^{\alpha} = \mathbf{e}_3 \tag{61}$$

with slips γ^α independent of x_3. All other slip systems are ignored. This approximate assumption is widely used in the literature under plane strain, as it allows for constructing simple 2D constitutive models. Using this assumption, it can be shown that:

$$\mathbf{e}_3 \cdot \boldsymbol{\nabla}\gamma^\alpha = 0 \quad \text{and} \quad \mathbf{l}^\alpha = \mathbf{m}^\alpha \times \mathbf{s}^\alpha = -\mathbf{e}_3 \tag{62}$$

which implies that screw dislocations vanish:

$$\rho^\alpha_\odot = \mathbf{l}^\alpha \cdot \boldsymbol{\nabla}\gamma^\alpha = 0, \quad \forall\, \alpha \in \{1,\, 2,\, ...,\, q\} \tag{63}$$

Ignoring the crystalline elastic anisotropy and using the proposed form of defect energy (34), with only edge dislocation densities, the energetic macroscopic and microscopic stresses involved in the simplified model can be expressed as:

$$\begin{array}{rcl} \boldsymbol{\sigma} & = & \lambda\, \mathrm{tr}\,(\boldsymbol{\varepsilon}_e)\, \mathbf{I} + 2\,\mu\, \boldsymbol{\varepsilon}_e \\ \pi^\alpha_{en} & = & 0 \\ \boldsymbol{\xi}^\alpha_{en} & = & X_0\, l^n_{en} \left[|\mathbf{s}^\alpha \cdot \boldsymbol{\nabla}\gamma^\alpha|^{n-2}\, \mathbf{s}^\alpha \otimes \mathbf{s}^\alpha \right] \cdot \boldsymbol{\nabla}\gamma^\alpha \end{array} \tag{64}$$

where λ and μ are the first and second Lamé elastic moduli. Concerning the dissipative microscopic stresses, simplified equations obtained from (51) and (52), with the slip resistances S^α_π and S^α_ξ assumed to evolve linearly with the effective plastic strains, are used to define these stresses:

$$\begin{array}{rcl} \pi^\alpha_{dis} & = & S^\alpha_\pi \left[\dfrac{\dot{e}^\alpha_\pi}{\dot{\gamma}^\alpha_0} \right]^m \dfrac{\dot{\gamma}^\alpha}{\dot{e}^\alpha_\pi} \\ \boldsymbol{\xi}^\alpha_{dis} & = & S^\alpha_\xi\, l^2_{dis} \left[\dfrac{\dot{e}^\alpha_\xi}{\dot{\gamma}^\alpha_0} \right]^m \dfrac{\boldsymbol{\nabla}^\alpha \dot{\gamma}^\alpha}{\dot{e}^\alpha_\xi} \end{array} \tag{65}$$

where, for $i \in \{\pi,\, \xi\}$:

$$\dot{S}^\alpha_i = \sum_{\beta=1}^{q} H_i\, \dot{e}^\beta_i \quad \text{with} \quad S^\alpha_i\,(0) = S_{i0},\ H_i = \text{constant} \geq 0 \tag{66}$$

Note that $S_{\pi 0} > 0$ and $S_{\xi 0} \geq 0$.

In summary, the overall constitutive equations of the simplified 2D SGCP model are:

$$\left\{ \begin{array}{l} \boldsymbol{\sigma} = \lambda\, \mathrm{tr}\,(\boldsymbol{\varepsilon}_e)\, \mathbf{I} + 2\,\mu\, \boldsymbol{\varepsilon}_e \\ \boldsymbol{\xi}^\alpha = X_0\, l^n_{en} \left[|\mathbf{s}^\alpha \cdot \boldsymbol{\nabla}\gamma^\alpha|^{n-2}\, \mathbf{s}^\alpha \otimes \mathbf{s}^\alpha \right] \cdot \boldsymbol{\nabla}\gamma^\alpha + S^\alpha_\xi\, l^2_{dis} \left[\dfrac{\dot{e}^\alpha_\xi}{\dot{\gamma}^\alpha_0} \right]^m \dfrac{\boldsymbol{\nabla}^\alpha \dot{\gamma}^\alpha}{\dot{e}^\alpha_\xi} \\ \pi^\alpha = S^\alpha_\pi \left[\dfrac{\dot{e}^\alpha_\pi}{\dot{\gamma}^\alpha_0} \right]^m \dfrac{\dot{\gamma}^\alpha}{\dot{e}^\alpha_\pi} \\ \dot{S}^\alpha_\pi = \displaystyle\sum_{\beta=1}^{q} H_\pi\, \dot{e}^\beta_\pi\,, \quad S^\alpha_\pi\,(0) = S_{\pi 0} > 0 \\ \dot{S}^\alpha_\xi = \displaystyle\sum_{\beta=1}^{q} H_\xi\, \dot{e}^\beta_\xi\,, \quad S^\alpha_\xi\,(0) = S_{\xi 0} \geq 0 \\ \dot{e}^\alpha_\pi = |\dot{\gamma}^\alpha|\,, \quad \dot{e}^\alpha_\xi = \|l_{dis}\, \boldsymbol{\nabla}^\alpha \dot{\gamma}^\alpha\| \\ \alpha = 1,\, 2,\, ...,\, q \end{array} \right. \tag{67}$$

These equations are solved numerically within the framework of finite element method. A brief presentation of the numerical procedure is presented in the next subsection.

3.2. Numerical implementation

The weak forms of the macroscopic and microscopic balance equations (first lines of systems (16) and (20)) may be formulated using the virtual power relations given in section 2. Here, the virtual fields $\delta\dot{\mathbf{u}}$ and $\delta\dot{\boldsymbol{\gamma}}$, which are referred to as test fields, are assumed to be kinematically admissible to $\mathbf{0}$ on the portions of the boundary of the studied domain on which Dirichlet (essential) boundary conditions are imposed. The macroscopic and microscopic weak forms can then be respectively expressed as:

$$\begin{aligned} G_u &= \int_{\mathcal{V}} \delta\dot{\boldsymbol{\varepsilon}} : \boldsymbol{\sigma}\, dv - \int_{\mathcal{S}_t} \delta\dot{\mathbf{u}} \cdot \mathbf{t}\, ds \\ G_\gamma &= \sum_{\alpha=1}^{q} \int_{\mathcal{V}} \boldsymbol{\nabla}\delta\dot{\gamma}^\alpha \cdot \boldsymbol{\xi}^\alpha\, dv + \sum_{\alpha=1}^{q} \int_{\mathcal{V}} \delta\dot{\gamma}^\alpha\, \pi^\alpha\, dv - \sum_{\alpha=1}^{q} \int_{\mathcal{V}} \delta\dot{\gamma}^\alpha\, \mathbf{P}^\alpha : \boldsymbol{\sigma}\, dv - \sum_{\alpha=1}^{q} \int_{\mathcal{S}_\chi^\alpha} \delta\dot{\gamma}^\alpha\, \chi^\alpha\, ds \end{aligned} \tag{68}$$

where $\mathcal{S}_t$ and $\mathcal{S}_\chi^\alpha$ are respectively the portions of the domain boundary on which macroscopic and microscopic traction forces, respectively noted as $\mathbf{t}$ and χ^α, are imposed.

To numerically solve these weak forms, a User-ELement (UEL) subroutine is implemented within the commercial finite element package ABAQUS/Standard. Both displacement and plastic slip fields ($\mathbf{u}$ and $\boldsymbol{\gamma}$) are considered as degrees of freedom in the UEL. Isoparametric two-dimensional eight-node quadratic elements are used. Integration within these elements is carried out using 9-point Gaussian technique. In each element, displacement fields u_i ($i \in \{1,\, 2\}$) and plastic slip fields γ^α ($\alpha \in \{1,\, 2,\, ...,\, q\}$) are approximated based on nodal values as follows:

$$u_i\,(x_1, x_2) = \sum_{k=1}^{8} N_k\,(x_1, x_2)\; U_i^k, \quad \gamma^\alpha\,(x_1, x_2) = \sum_{k=1}^{8} N_k\,(x_1, x_2)\; \Gamma_k^\alpha \tag{69}$$

where U_i^k and Γ_k^α are respectively the nodal values of displacement u_i and plastic slip γ^α, and N_k are the interpolation (shape) functions, which are assumed to be the same for both displacement and plastic slip fields. Using these field approximations, the above weak forms can be written, in matrix form, within a representative finite element as:

$$\begin{aligned} G_u^e &= \left(\delta\underline{\dot{U}}^e\right)^T \cdot \left(\int_{\mathcal{V}^e} \underline{\underline{B}}_u^T \cdot \underline{\sigma}\, dv - \int_{\mathcal{S}_t^e} \underline{\underline{N}}_u^T \cdot \underline{t}\, ds \right) \\ G_\gamma^e &= \left(\delta\underline{\dot{\Gamma}}^e\right)^T \cdot \left(\int_{\mathcal{V}^e} \underline{\underline{B}}_\gamma^T \cdot \underline{\xi}\, dv + \int_{\mathcal{V}^e} \underline{\underline{N}}_\gamma^T \cdot \underline{\pi}\, dv - \int_{\mathcal{V}^e} \underline{\underline{N}}_\gamma^T \cdot \underline{\tau}\, dv - \int_{\mathcal{S}_\chi^e} \underline{\underline{N}}_\gamma^T \cdot \underline{\chi}\, ds \right) \end{aligned} \tag{70}$$

where $\underline{\sigma}$, $\underline{\pi}$ and $\underline{\xi}$ are vector representations of the macroscopic stress and the microscopic stresses on all slip systems, $\underline{\tau}$ is a vector containing the resolved shear stresses on all slip systems, $\underline{t}$ is the macroscopic traction vector, $\underline{\chi}$ is a vector containing the microscopic tractions on all slip systems, $\underline{\underline{N}}_u$ and $\underline{\underline{B}}_u$ are interpolation and gradient matrices associated with the displacement field, and $\underline{\underline{N}}_\gamma$ and $\underline{\underline{B}}_\gamma$ are interpolation and gradient matrices associated with the plastic slip fields. Expressions of these vector and matrix quantities are long and not revealing, they are not presented in this paper.

The principle of virtual power implies that G_u^e and G_γ^e are zero for any virtual variations of the element nodal variables $\delta\underline{\dot{U}}^e$ and $\delta\underline{\dot{\Gamma}}^e$. Therefore:

$$\begin{aligned} \underline{R}_u^e &= \int_{\mathcal{V}^e} \underline{\underline{B}}_u^T \cdot \underline{\sigma}\, dv - \int_{\mathcal{S}_t^e} \underline{\underline{N}}_u^T \cdot \underline{t}\, ds &&= \underline{0} \\ \underline{R}_\gamma^e &= \int_{\mathcal{V}^e} \underline{\underline{B}}_\gamma^T \cdot \underline{\xi}\, dv + \int_{\mathcal{V}^e} \underline{\underline{N}}_\gamma^T \cdot \underline{\pi}\, dv - \int_{\mathcal{V}^e} \underline{\underline{N}}_\gamma^T \cdot \underline{\tau}\, dv - \int_{\mathcal{S}_\chi^e} \underline{\underline{N}}_\gamma^T \cdot \underline{\chi}\, ds &&= \underline{0} \end{aligned} \tag{71}$$

These equations are linearized with respect to the variations of the element nodal variables $\underline{U}^e$ and $\underline{\Gamma}^e$, which results in an elementary system of linear equations that can be presented in matrix form as follows:

$$\begin{bmatrix} \underline{\underline{K}}^e_{uu} & \underline{\underline{K}}^e_{u\gamma} \\ \underline{\underline{K}}^e_{\gamma u} & \underline{\underline{K}}^e_{\gamma\gamma} \end{bmatrix} \begin{bmatrix} \Delta\underline{U}^e \\ \Delta\underline{\Gamma}^e \end{bmatrix} = \begin{bmatrix} -\underline{R}^e_u \\ -\underline{R}^e_\gamma \end{bmatrix} \tag{72}$$

where:

$$\underline{\underline{K}}^e_{uu} = \frac{\partial \underline{R}^e_u}{\partial \underline{U}^e}, \quad \underline{\underline{K}}^e_{u\gamma} = \frac{\partial \underline{R}^e_u}{\partial \underline{\Gamma}^e}, \quad \underline{\underline{K}}^e_{\gamma u} = \frac{\partial \underline{R}^e_\gamma}{\partial \underline{U}^e}, \quad \underline{\underline{K}}^e_{\gamma\gamma} = \frac{\partial \underline{R}^e_\gamma}{\partial \underline{\Gamma}^e} \tag{73}$$

The global system of linear equations can be obtained by assembling all the elementary systems associated with the overall finite elements. This system is solved by means of a Newton-Raphson iterative solution scheme for the overall increments of the displacement and plastic slip fields ($\Delta\underline{U}$ and $\Delta\underline{\Gamma}$, respectively). At each iteration, updated values of these increments are obtained and used to numerically solve the constitutive equations (67) at the Gauss points (algorithm 1).

Algorithm 1 Time integration of the SGCP constitutive equations

Inputs: Δt, $\Delta\mathbf{u}$, $\Delta\boldsymbol{\gamma}$, $\mathbf{u}$, $\boldsymbol{\gamma}$, $\boldsymbol{\varepsilon}$, $\boldsymbol{\varepsilon}_e$, $\boldsymbol{\varepsilon}_p$, $\boldsymbol{\sigma}$, S^α_π, S^α_ξ, π^α, $\boldsymbol{\xi}^\alpha$

Compute: $\Delta\boldsymbol{\varepsilon} = [\nabla(\Delta\mathbf{u})]_{sym}$, $\quad \Delta\boldsymbol{\varepsilon}_p = \sum_{\alpha=1}^{q} \Delta\gamma^\alpha \boldsymbol{P}^\alpha$, $\quad \Delta\boldsymbol{\varepsilon}_e = \Delta\boldsymbol{\varepsilon} - \Delta\boldsymbol{\varepsilon}_p$

Update: $\mathbf{u} \leftarrow \mathbf{u} + \Delta\mathbf{u}$, $\quad \boldsymbol{\gamma} \leftarrow \boldsymbol{\gamma} + \Delta\boldsymbol{\gamma}$, $\quad \boldsymbol{\varepsilon} \leftarrow \boldsymbol{\varepsilon} + \Delta\boldsymbol{\varepsilon}$, $\quad \boldsymbol{\varepsilon}_e \leftarrow \boldsymbol{\varepsilon}_e + \Delta\boldsymbol{\varepsilon}_e$, $\quad \boldsymbol{\varepsilon}_p \leftarrow \boldsymbol{\varepsilon}_p + \Delta\boldsymbol{\varepsilon}_p$

Compute: $\boldsymbol{\sigma} = \lambda\,\mathrm{tr}(\boldsymbol{\varepsilon}_e)\,\mathbf{I} + 2\,\mu\,\boldsymbol{\varepsilon}_e$

for α=1 **to** q **do**

  Compute: $\Delta e^\alpha_\pi = |\Delta\gamma^\alpha|$, $\quad \Delta e^\alpha_\xi = \|l_{dis}\,\boldsymbol{\nabla}^\alpha(\Delta\gamma^\alpha)\|$

end for

for α=1 **to** q **do**

  Compute: $\Delta S^\alpha_\pi = \sum_{\beta=1}^{q} H_\pi\,\Delta \mathrm{e}^\beta_\pi$, $\quad \Delta S^\alpha_\xi = \sum_{\beta=1}^{q} H_\xi\,\Delta e^\beta_\xi$

  Update: $S^\alpha_\pi \leftarrow S^\alpha_\pi + \Delta S^\alpha_\pi$, $\quad S^\alpha_\xi \leftarrow S^\alpha_\xi + \Delta S^\alpha_\xi$

  Compute: $\pi^\alpha = S^\alpha_\pi \left[\dfrac{\Delta e^\alpha_\pi}{\dot\gamma^\alpha_0\,\Delta t}\right]^m \dfrac{\Delta\gamma^\alpha}{\Delta e^\alpha_\pi}$

  Compute: $\boldsymbol{\xi}^\alpha = X_0\,l^n_{en}\left[|\mathbf{s}^\alpha\cdot\boldsymbol{\nabla}\gamma^\alpha|^{n-2}\,\mathbf{s}^\alpha\otimes\mathbf{s}^\alpha\right]\cdot\boldsymbol{\nabla}\gamma^\alpha + S^\alpha_\xi\,l^2_{dis}\left[\dfrac{\Delta e^\alpha_\xi}{\dot\gamma^\alpha_0\,\Delta t}\right]^m \dfrac{\boldsymbol{\nabla}^\alpha(\Delta\gamma^\alpha)}{\Delta e^\alpha_\xi}$

end for

4. Assessment and parametric investigation of the SGCP model

To investigate the influence of the major constitutive parameters involved in the proposed SGCP model, the simplified 2D version of this model is applied to simulate simple 2D shear tests. These tests have been widely treated by existing strain gradient plasticity models and interesting comparison results related to these tests exist in the literature (*e.g.*, Shu et al., 2001; Bittencourt et al., 2003; Niordson and Hutchinson, 2003; Gurtin et al., 2007; Nellemann et al., 2017). A 2D crystalline strip of height h and width w is considered, with two active slip systems symmetrically oriented with respect to $\mathbf{e}_1$ direction ($\theta_1 = -\theta_2 = 60°$), as illustrated in Fig. 1. This strip is discretized using 100 quadratic finite elements, which represents a good compromise between results accuracy and computation cost. To model the infinite length of the strip in $\mathbf{e}_1$

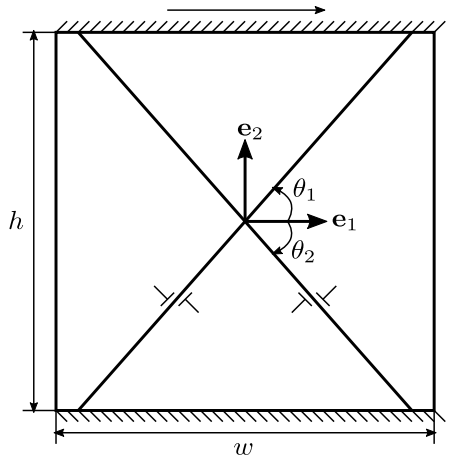

Fig. 1. 2D crystalline strip with two active slip systems, symmetrically tilted by $\theta_1 = 60°$ and $\theta_2 = -60°$ with respect to $\mathbf{e}_1$ direction, for shear test simulations.

direction, the following periodic conditions are imposed on the left and right edges:

$$\begin{array}{l} u_i\left(0, x_2, t\right) = u_i\left(w, x_2, t\right), \quad \text{for } i = 1,\, 2 \\ \gamma^\alpha\left(0, x_2, t\right) = \gamma^\alpha\left(w, x_2, t\right), \quad \text{for } \alpha = 1,\, 2 \end{array} \tag{74}$$

In addition, the bottom edge is subject to macro-clamped displacement boundary conditions and the top edge is subject to a loading-unloading cycle of displacement in $\mathbf{e}_1$ direction:

$$u_1(x_1, 0, t) = u_2(x_1, 0, t) = 0,\ u_1(x_1, h, t) = h\Gamma\left(t\right), \text{ and } u_2(x_1, h, t) = 0 \tag{75}$$

where $\Gamma\left(t\right)$ is the prescribed shear strain, going from 0 to 0.02 and back to 0. In order to establish proportional and non-proportional loading conditions, which are necessary to better investigate certain SGCP aspects, two types of microscopic (slip) boundary conditions are also considered on the top and bottom edges. In the case of proportional loading, both the edges are passivated from the beginning to the end of the simulation:

$$\gamma^\alpha(x_1, 0, t) = \gamma^\alpha(x_1, h, t) = 0, \quad \text{for } \alpha = 1,\, 2 \tag{76}$$

However, in the case of non-proportional loading, only the bottom edge is passivated over the entire simulation. The top edge is assumed to be unpassivated until a certain value of the prescribed shear strain in the plastic range ($\Gamma = 0.01$) and then passivated until the end of the simulation:

$$\gamma^\alpha(x_1, 0, t) = 0,\ \dot{\gamma}^\alpha\left(x_1, h, t > t_0\right) = 0, \quad \text{for } \alpha = 1,\, 2 \tag{77}$$

where t_0 is the passivation time, *i.e.,* time at which $\Gamma\left(t_0\right) = 0.01$. Note that, in the considered case of non-proportional loading, nonuniform plastic strain distribution develops within the strip before the non-proportional loading source (top edge passivation) occurs. As will be seen later, this allows for a more complete investigation of the higher-order energetic and dissipative effects under non-proportional loading conditions.

Results in terms of macroscopic stress-strain curves and plastic shear strain distributions in $\mathbf{e}_2$ direction are adopted to investigate the influence of the major constitutive parameters on the global response of the considered material, with a focus on those implied in the definition of the higher-order energetic and dissipative stresses. The stress-strain curves are generated based on the average shear stress within the strip (simply noted σ_{12} hereafter) as a function of the prescribed shear strain Γ. For the plastic shear strain distribution in

Tab. 1. Material parameters implied in system (67): the values of the fixed parameters are taken from Gurtin et al. (2007), for comparison purposes.

Material parameter name	Symbol	Value	Unit
First Lamé elastic modulus	λ	150	GPa
Second Lamé elastic modulus	μ	100	GPa
Reference slip rate	$\dot{\gamma}_0^\alpha$	0.04	s^{-1}
Rate-sensitivity parameter	m	0.05	–
Higher-order energetic slip resistance	X_0	50	MPa
Initial first-order dissipative slip resistance	$S_{\pi 0}$	50	MPa
Initial higher-order dissipative slip resistance	$S_{\xi 0}$	case study	MPa
First-order hardening modulus	H_π	case study	MPa
Higher-order hardening modulus	H_ξ	case study	MPa
Energetic length scale	l_{en}	case study	μm
Dissipative length scale	l_{dis}	case study	μm
Defect energy index	n	case study	–

$\mathbf{e}_2$ direction, the engineering plastic shear strain $\gamma_{12}^p = 2\,\varepsilon_{12}^p$ is employed. These results are mainly discussed with respect to the results of Gurtin et al. (2007), whose theory is used as basis of the present one. Therefore, the material parameters that are not concerned by the parametric investigation in system (67) are set equal to those used by Gurtin et al. (2007), as illustrated in Tab. 1.

4.1. Influence of higher-order energetic stress parameters

In this subsection, the influence of the main higher-order energetic stress parameters, specifically the energetic length scale l_{en} and the defect energy index n, and the interaction between them are investigated in the absence of dissipative effects. For this purpose, the dissipative length scale l_{dis} and the first-order hardening modulus H_π are set to zero.

4.1.1. Energetic length scale l_{en}: validation of the model implementation

Using $l_{dis} = 0$, the higher-order effective plastic strain rates $\dot{e}_\xi^\alpha$ (41) vanish and the first-order counterparts $\dot{e}_\pi^\alpha$ (40) coincide with the coupled measures proposed by Gurtin et al. (2007):

$$\dot{d}^\alpha = \sqrt{(\dot{e}_\pi^\alpha)^2 + \left(\dot{e}_\xi^\alpha\right)^2} = \dot{e}_\pi^\alpha, \qquad \text{for } \alpha = 1,\, 2 \tag{78}$$

Therefore, by using the same values of constitutive parameters, the present model becomes equivalent to the Gurtin et al. (2007) model. Comparison between the results of the two models in this case allows for validation of the numerical implementation of present one. Fig. 2 presents the comparison results for different values of l_{en}, obtained using quadratic defect energy ($n = 2$) and proportional loading. The present results are in very good agreement with the results of Gurtin et al. (2007), regardless of the l_{en} value. The very small differences between the results would be due to the use of different types of finite elements and different mesh refinements. As mentioned earlier, 8-node quadratic elements are used in this work, whereas 9-node quadratic elements are adopted in the work of Gurtin et al. (2007). As expected, for quadratic defect energy ($n = 2$) and proportional loading conditions, the energetic length scale l_{en} contributes to hardening but not to strengthening. By varying l_{en}, only the hardening rate after yielding changes, the plastic regime always starts from the same yield point (Fig. 2a). The case of $l_{en} = 0$ corresponds to the classical crystal plasticity (CP) with no hardening. This case, which will simply be designated by "Perfect CP" in subsequent figures, leads to a flat stress-strain curve with no hardening after yielding and to a uniform plastic shear strain distribution through the strip thickness. For $l_{en} = 0.7\,h$ and $l_{en} = h$, kinematic hardening occurs, leading to

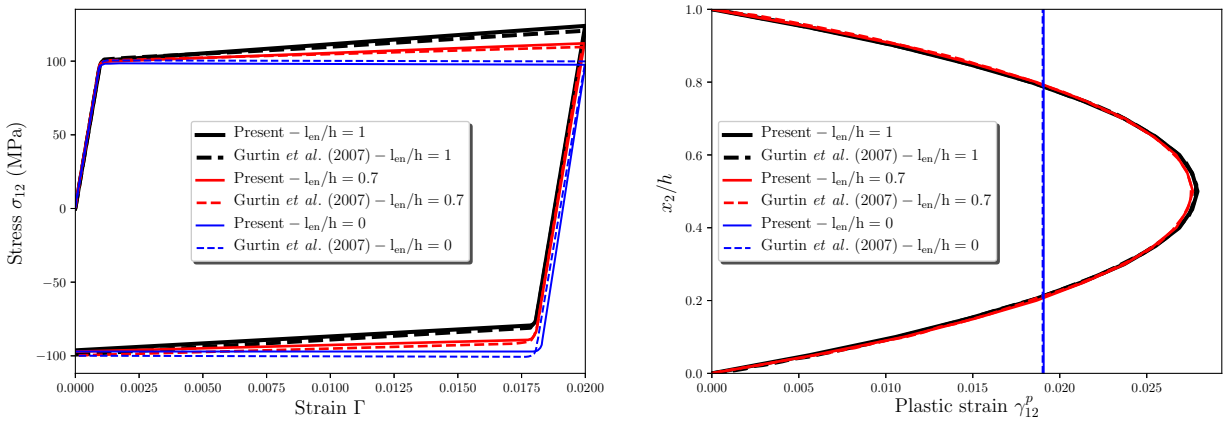

(a) Stress-strain curves

(b) Plastic shear strain distributions along $\mathbf{e}_2$ direction

Fig. 2. Influence of the energetic length scale l_{en} under proportional loading conditions in the absence of higher-order dissipative effects: comparison between the present and Gurtin et al. (2007) results ($n = 2$, $l_{dis} = 0$, $H_\pi = 0$).

classical Bauschinger effects which become more marked with increasing l_{en}. The associated plastic shear strain distributions along the strip thickness present a quadratic form (Fig. 2b).

4.1.2. Defect energy index n: investigation under proportional and non-proportional loading conditions

In the above l_{en} investigation, quadratic defect energy is employed ($n = 2$) with only proportional loading conditions. The obtained results confirm a common belief that l_{en} only contributes to material hardening (Gurtin et al., 2007). However, it has recently been demonstrated that this belief is not necessarily true for other forms of defect energy (Fleck and Willis, 2015; Wulfinghoff et al., 2015; Forest et al., 2019). Using two different defect energy formulations, El-Naaman et al. (2019) have recently conducted an interesting investigation into the interaction between the energetic length scale effects and the form of the defect energy. The obtained results highlight the complex nonlinear hardening effects of l_{en} in the case of non-quadratic defect energy, resulting in an apparent material strengthening under monotonic loading. However, only proportional loading conditions are used in their investigation. Hereafter, it is proposed to extend this investigation by considering both proportional and non-proportional loading conditions.

Fig. 3 presents the stress-strain curves for different values of $n < 2$ and l_{en}, obtained under the proportional and non-proportional loading conditions introduced at the beginning of the section. By analyzing only the loading part of the results, l_{en} seems to contribute to material strengthening. Strengthening (elastic gap at initial yield) is observed in both the proportional and non-proportional loading cases. The smaller the value of n (*i.e.*, n approaches 1), the larger are the gaps. Under the considered non-proportional loading conditions, the obtained elastic gaps at initial yield are less marked than those obtained under proportional loading conditions. Moreover, at the occurrence of the non-proportional loading source (passivation of the top edge), no further elastic gaps are observed, there is only a short rapid rise in the average stress with a slope much smaller than the elastic slope (Fig. 3b). With only the bottom edge passivated from the beginning, lower plastic strain gradients develop within the strip, which explains the smaller elastic gaps at initial yield. After yielding, the plastic strain gradients continue to develop over a large part of the strip and their existence prior to the top edge passivation prevents the occurrence of further gaps. Considering now the entire loading-unloading results, two striking features can be noticed. The first feature, which is concerned with both the proportional and non-proportional loading cases, is the concave form of the unloading curves. The second feature, which is concerned with only the non-proportional loading case, is the presence of inflection points at the middle of the associated unloading curves. Interestingly, these inflection points seem to occur

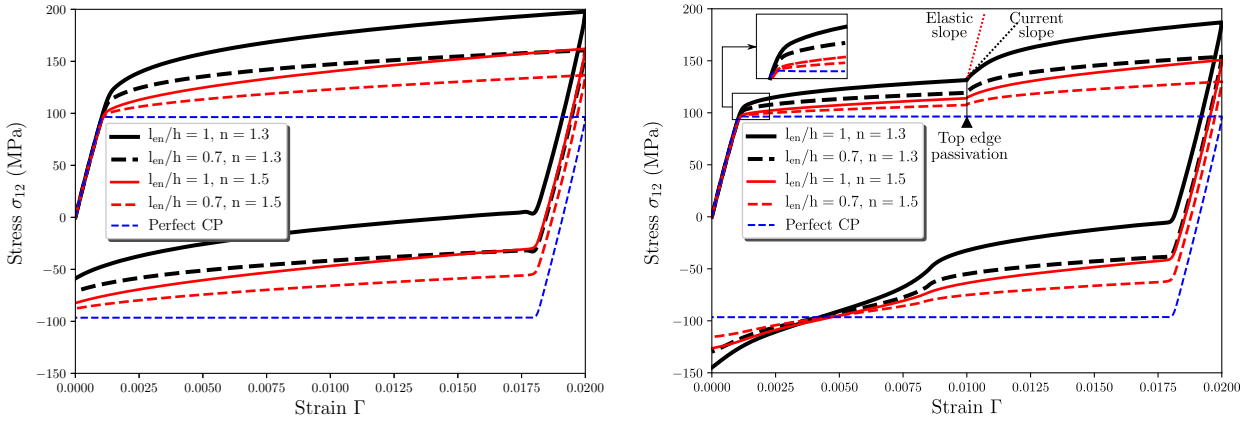

(a) Proportional loading conditions

(b) Non-proportional loading conditions

Fig. 3. Stress-strain responses under proportional and non-proportional loading conditions for different values of the defect energy index n in the range of $n < 2$ and different values of the energetic length scale l_{en} ($l_{dis} = 0$, $H_\pi = 0$).

at approximately the same plastic states at which the top edge was passivated, even though no modification is made to the unloading conditions.

To better understand these features, more complete simulations under proportional and non-proportional loading conditions were performed, using $n = 1.3$ and $l_{en} = h$. In these simulations, after a first (proportional or non-proportional) loading to a macroscopic shear strain $\Gamma = 0.02$, a complete loading cycle is applied, such that Γ goes from 0.02 to -0.02 and back to 0.02 (*i.e.,* the simple unloading $\Gamma = 0.02 \rightarrow 0$ is replaced by a complete cycle $\Gamma = 0.02 \rightarrow -0.02 \rightarrow 0.02$). Fig. 4 presents the associated results in terms of stress-strain responses and plastic slip distributions at key stages of the loading cycle. The stress-strain response associated with the proportional case shows that the material only experienced an unusual pure nonlinear kinematic hardening with steep-sloped inflection points (Fig. 4a). These inflection points occur at zero plastic slips where the plastic slip gradients vanish (Stage 4 in Fig. 4b). They are caused by a rapid increase followed by a rapid decrease in the evolution rate of the higher-order energetic stresses $\boldsymbol{\xi}^{\alpha}_{en}$ as the latter approach their singularity at zero plastic slip gradients. The obtained stress-strain response under proportional loading confirms the results of El-Naaman et al. (2019). Further discussion on this response can be found in their paper. For the non-proportional case, more complex stress-strain response is obtained with additional inflections points (Fig. 4a). Each of the (steep-sloped) inflection points observed in the proportional case is split into two moderate-sloped ones. As can be noted from Fig. 4c, one of these moderate-sloped inflection points takes place at plastic slips in the vicinity of the top edge equivalent to those measured at this edge at its passivation, reflecting a loading history memory-like effect of l_{en}. This point corresponds to nearly zero plastic slip gradients in the upper half of the studied strip (Stage $4'$ in Fig. 4c). The other moderate-sloped inflection point occurs at zero plastic slips in the vicinity of the bottom edge where nearly zero plastic slip gradients occur in the lower half of the strip (Stage $7'$ in Fig. 4c). With different passivation conditions applied on the top and bottom edges, the plastic slip gradients do not vanish at the same time in the upper and lower strip halves, leading to two distinct and smoother inflections points.

The nonlinear kinematic hardening with inflection points, which is observed under proportional and non-proportional loading conditions, is largely controlled by the defect energy index n (Fig. 3). It becomes less and less marked as n approaches 2. From $n = 2$, this hardening type disappears and is replaced by the classical kinematic hardening with no apparent inflection points (Fig. 5). In this case, l_{en} has no longer any contribution to material strengthening, neither under proportional loading nor under non-proportional

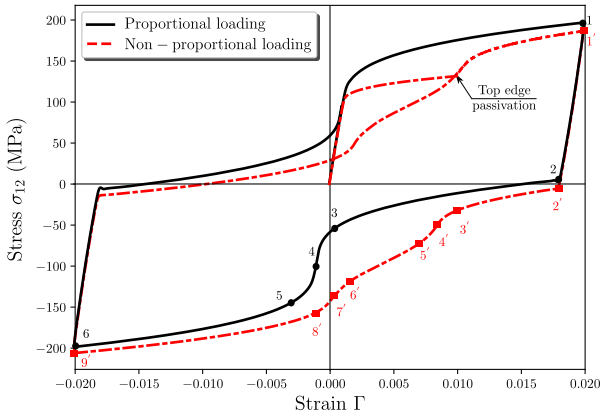

(a) Stress-strain curves

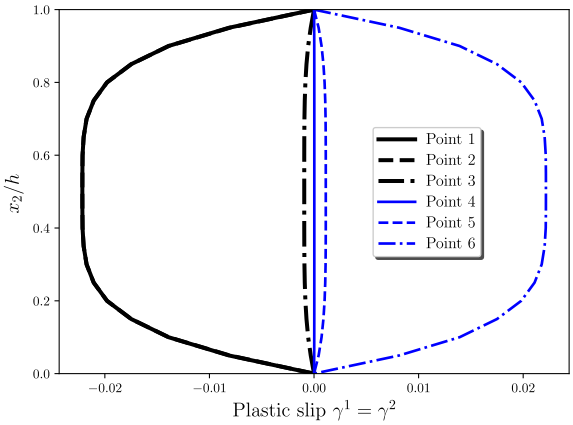

(b) Plastic slip distributions at stages 1 to 6 in Fig. 4a

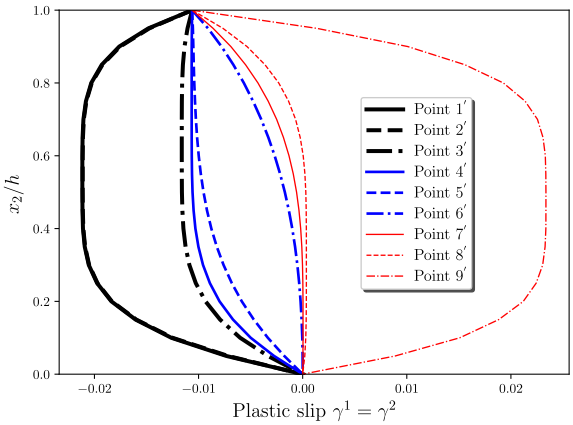

(c) Plastic slip distributions at stages $1'$ to $9'$ in Fig. 4a

Fig. 4. Stress-strain curves and plastic slip distributions at different loading stages, obtained under first proportional and non-proportional loading to a macroscopic shear strain $\Gamma = 0.02$ followed by a complete loading cycle $\Gamma = 0.02 \rightarrow -0.02 \rightarrow 0.02$ ($n = 1.3$, $l_{en} = h$, $l_{dis} = 0$, $H_\pi = 0$).

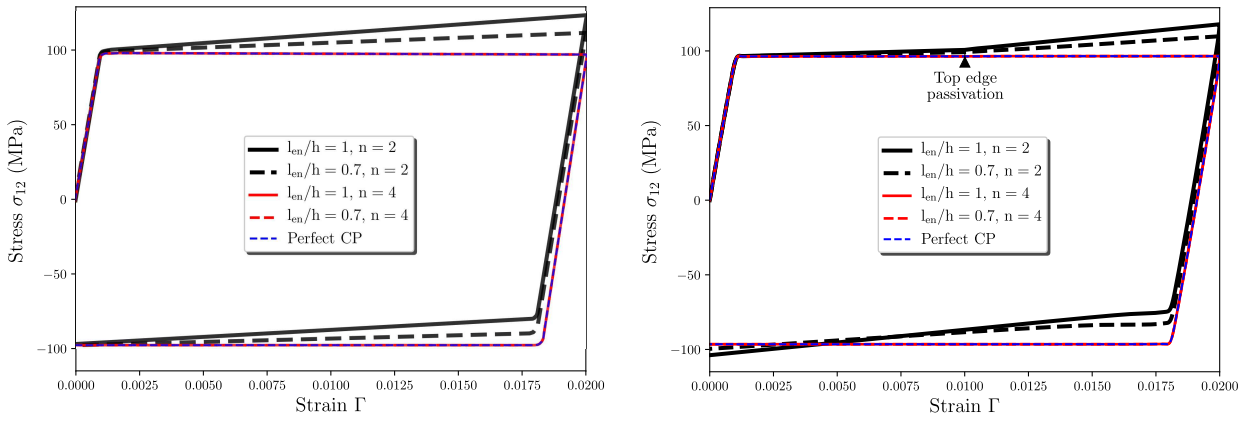

(a) Proportional loading conditions

(b) Non-proportional loading conditions

Fig. 5. Stress-strain responses for different values of the defect energy index n in the range of $n \geq 2$ and different values of the energetic length scale l_{en}, obtained under proportional and non-proportional loading conditions ($l_{dis} = 0$, $H_\pi = 0$).

loading. For the latter type of loading, the top edge passivation is only marked by a change in the hardening rate to match that corresponding to proportional loading with the top and bottom edges passivated from the beginning. In the range of $n \geq 2$, l_{en} has only effects on the rate of the classical kinematic hardening, which decrease with increasing n. A large value of n can even cancel these effects of l_{en} (case of $n = 4$ in Fig. 5).

In the framework of SGCP, the unusual nonlinear kinematic hardening, at least that obtained under proportional loading, was first reported by Ohno et al. (2009), using rank-one defect energy. However, the authors did not recognize the physical origin of this phenomenon. Instead, they further developed their model to replace the rank-one defect energy by a dissipative formulation removing the inflection points. More recently, this phenomenon was also obtained by several authors using other forms of defect energy (Wulfinghoff et al., 2015; Forest et al., 2019; El-Naaman et al., 2019). Wulfinghoff et al. (2015) were the first to provide a physical explanation to the phenomenon in the context of SGCP. According to them, it corresponds to the kinematic hardening type III (KIII) of Asaro (1975). This type is associated with a "first in/last out" sequence of dislocation motion and represents the most perfect form of recovery of plastic memory. Although uncommon, experimental evidence of the obtained nonlinear kinematic hardening exists in the literature. Unusual stress-strain hysteresis loops with inflection points have already been observed in some Al-Cu-Mg and Fe-Cr polycrystalline alloys (Stoltz and Pelloux, 1976; Taillard and Pineau, 1982). An illustration of these loops, which is obtained by Taillard and Pineau (1982) in a large-grained Fe-Cu alloy aged at 923 K for 72 h after one loading cycle, is given in Fig. 6. TEM observations by Stoltz and Pelloux (1976) and Taillard and Pineau (1982) show that the inflected loops are caused by the piling-up of dislocations at the precipitates and their possible destruction under reverse loading. These experimentally observed mechanisms are analogous to the piling-up and unpiling-up of dislocations at the passivated edges in the present simulations. The use of non-quadratic defect energy with $n < 2$ seems to provide an accurate continuum description of the piling-up and unpiling-up phenomena. This results in plastic shear strain distributions more in consistency with small scale predictions using dislocation mechanics (*e.g.*, Shu et al., 2001). Fig. 7a gives the plastic shear strain profiles along the strip thickness for different values of n, obtained using proportional loading. Using $n < 2$, obvious boundary layers develop in the vicinity of the top and bottom boundaries with nearly uniform plastic shear strain distribution outside these layers, as generally predicted using discrete dislocations mechanics (*e.g.*, Shu et al., 2001). This would constitute another argument in favor of defect energy formulations with order-controlling index $n < 2$.

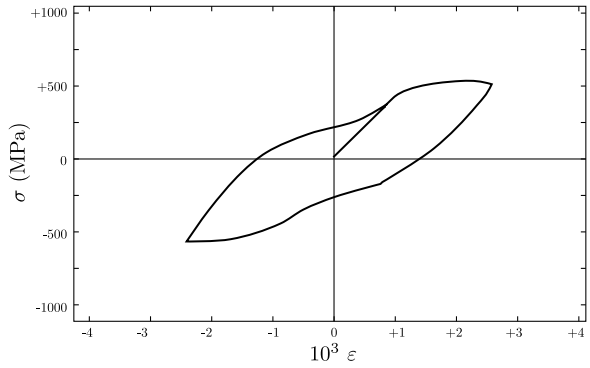

Fig. 6. Experimental evidence of the nonlinear kinematic hardening after one loading cycle in a large-grained Fe–Cr alloy aged at 923 K for 72 h (Reproduced from Taillard and Pineau (1982)).

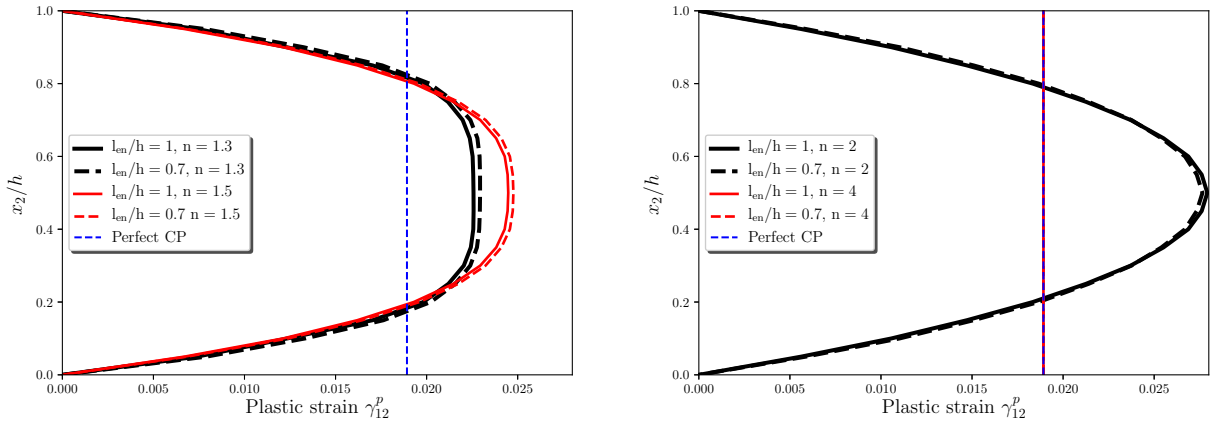

(a) Defect energy order-controlling index $n < 2$

(b) Defect energy order-controlling index $n \geq 2$

Fig. 7. Plastic shear strain distributions along $\mathbf{e}_2$ direction for different values of the defect energy order-controlling index n and different values of the energetic length scale l_{en}, obtained under proportional loading ($l_{dis} = 0$, $H_\pi = 0$).

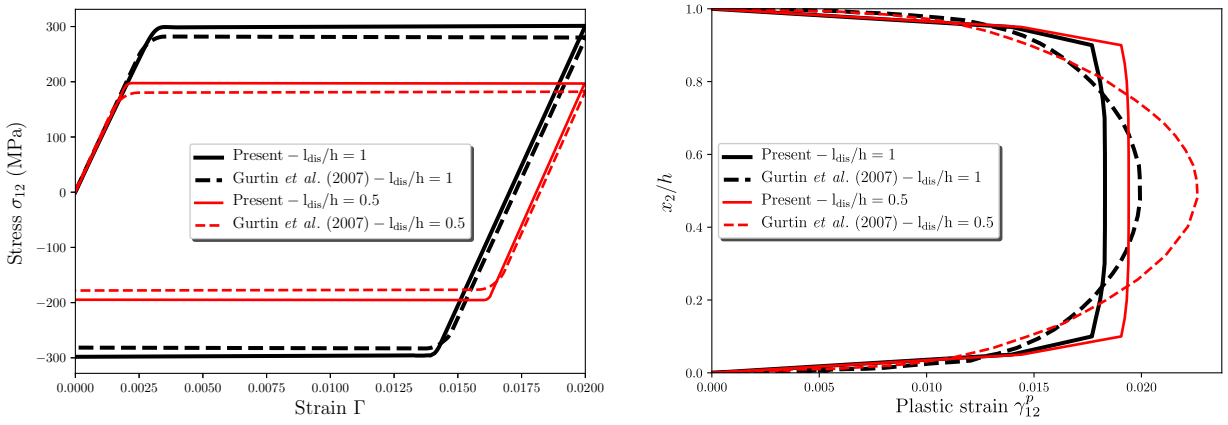

(a) Stress-strain curves

(b) Plastic shear strain distributions along $\mathbf{e}_2$ direction

Fig. 8. Influence of the dissipative length scale l_{dis} in the absence of higher-order energetic effects under proportional loading conditions: comparison between the present and Gurtin et al. (2007) results ($l_{en} = 0$, $S_{\xi 0} = 50\,\mathrm{MPa}$, $H_\pi = 0$, $H_\xi = 0$).

4.2. Influence of higher-order dissipative stress parameters

In this subsection, the main higher-order dissipative stress parameters are investigated in the framework of uncoupled dissipation. For a better analysis of these parameters, the energetic and first-order hardening effects are ignored (*i.e.,* $l_{en} = 0$ and $H_\pi = 0$).

4.2.1. Dissipative length scale l_{dis}: investigation of the uncoupled dissipation assumption

In this investigation, the initial higher-order dissipative slip resistance is set equal to the first-order one ($S_{\xi 0} = S_{\pi 0}$). Moreover, the higher-order hardening effects are first ignored ($H_\xi = H_\pi = 0$). By doing so, the only difference between the present and Gurtin et al. (2007) models lies in the way the effective plastic strain measures are calculated. Comparison between the results of the models in this case makes it possible to underscore the influence of the uncoupled dissipation assumption adopted in this work. Fig. 8 gives the comparison results for different values of dissipative length scale, obtained under proportional loading. These results are achieved by setting $S_{\xi 0} = S_{\pi 0} = 50\,\mathrm{MPa}$, which corresponds to the initial slip resistance used by Gurtin et al. (2007) in their study of l_{dis}. As can be seen in Fig. 8a, in terms of stress-strain response, the results are not particularly sensitive to the use of coupled or uncoupled formulation for the dissipation processes. Both the formulations lead to the same conclusions about the influence of l_{dis} on the material response. The parameter l_{dis} influences the yield strength, which increases with increasing l_{dis}, but not the strain hardening after yielding. A slight overestimation of the yield strength as predicted by the present SGCP model can however be reported. This overestimation is due to the fact that the uncoupled plastic strain measures lead to slightly smaller values, compared to those which can be obtained using coupled ones (Gurtin et al., 2007). This results in overestimating the higher-order dissipative stresses and then the energetic macroscopic stress $\boldsymbol{\sigma}$ via the flow rule (59).

Although leading to close results in terms of stress-strain curves, the assumption of uncoupled dissipation has a strong influence on the distribution of the plastic shear strain across the thickness. As illustrated in Fig. 8b, the plastic shear strain profiles obtained in this work are quite different from those obtained by Gurtin et al. (2007) using coupled dissipation. The latter profiles have always smooth parabolic forms with more or less sharp gradients in the vicinity of the top and bottom boundaries. With the hypothesis of uncoupled dissipation, more clearly distinguishable boundary layers develop in the vicinity of the top and bottom boundaries; beyond these layers, the plastic shear strain becomes near-uniform with a

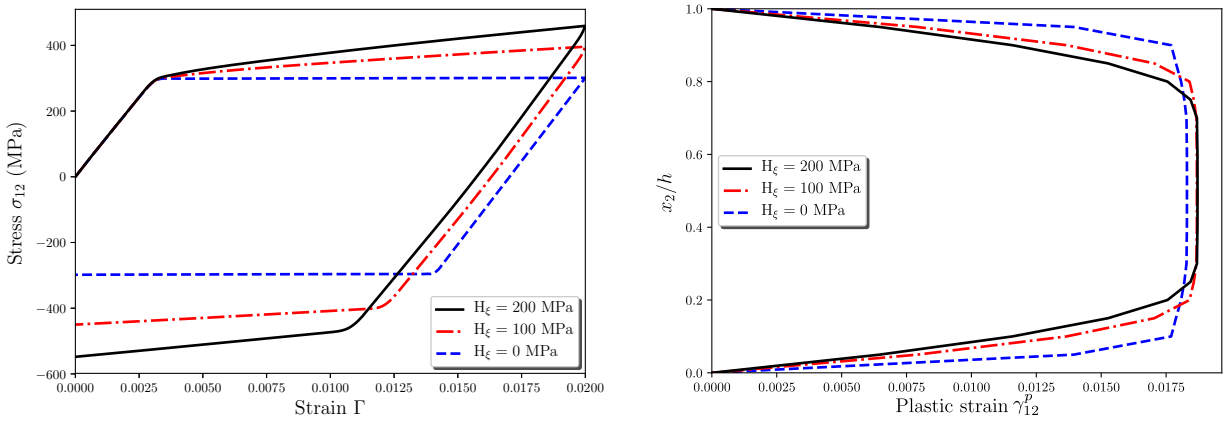

(a) Stress-strain curves

(b) Plastic shear strain distributions along $\mathbf{e}_2$ direction

Fig. 9. Influence of the higher-order hardening modulus H_ξ in the absence of higher-order energetic effects ($l_{en} = 0$, $l_{dis} = h$, $S_{\xi 0} = 50\,\mathrm{MPa}$, $H_\pi = 0$).

plateau-shaped distribution (Fig. 8b). With no higher-order hardening ($H_\xi = 0$), these layers present a very small thickness, which is in very good agreement with the results of Gurtin et al. (2007). The thickness of such layers can, however, be controlled by the higher-order hardening modulus H_ξ. Fig. 9 compares the stress-strain results and the associated plastic shear strain profiles with and without higher-order hardening ($H_\xi = 0,\ 100,\ 200\,\mathrm{MPa}$), obtained using proportional loading. The thickness of the obtained boundary layers depends on H_ξ. The larger this parameter, the thicker are the boundary layers (Fig. 9b). Such a parameter generates isotropic hardening effects of more or less standard type (Fig. 9a).

The plastic shear strain distributions obtained in this work using uncoupled dissipation seem to be more in consistency with small scale numerical predictions (*e.g.*, Bittencourt et al., 2003; Shu et al., 2001). Fig. 10 compares the plastic shear strain profiles predicted by the present model with those predicted by Shu et al. (2001) using discrete dislocation plasticity, for different values of applied shear strain Γ under proportional conditions. The material parameters used to obtain the present profiles are determined by identification procedure considering only dissipative stresses: $l_{en} = 0$, $S_{\pi 0} = 15\,\mathrm{MPa}$, $H_\pi = 0$, $l_{dis} = 0.3\,h$, $S_{\xi 0} = 3\,\mathrm{MPa}$, and $H_\xi = 200\,\mathrm{MPa}$. The obtained results are in good agreement with the results of Shu et al. (2001). The small differences between the results in the boundary layers at large applied shear strains Γ are due to the asymmetry of the discrete dislocation profiles, which is caused by the fluctuations in the plastic strains.

4.2.2. Initial higher-order dissipative slip resistance $S_{\xi 0}$: towards a more flexible control of elastic gaps

In the above l_{dis} study, the initial higher-order dissipative slip resistance is fixed at $S_{\xi 0} = S_{\pi 0} = 50\,\mathrm{MPa}$ and only proportional loading is applied. The obtained results highlight the contribution of l_{dis} to material strengthening, which increases with increasing l_{dis} (Fig. 8a), as noted in the literature using coupled dissipation. Further investigation into l_{dis} effects under varying $S_{\xi 0}$ is given hereafter, using proportional and non-proportional loading conditions.

Starting with the proportional loading conditions, Fig. 11a displays the associated stress-strain results for different values of $S_{\xi 0}$, with $l_{dis} = h$ and $H_\xi = 100\,\mathrm{MPa}$. At fixed l_{dis}, elastic gaps at initial yield are largely controlled by $S_{\xi 0}$. The smaller this parameter, the smaller are the gaps, which can also be removed by setting $S_{\xi 0} = 0$ (in practice, a small value must be used instead of 0 to avoid excessively small time steps for convergence). Using $S_{\xi 0} = 0.01\,\mathrm{MPa}$, no apparent elastic gaps are obtained at initial yield. This is in accordance with the outcomes of Fleck et al. (2015) and can be explained by zero (nearly zero) higher-order

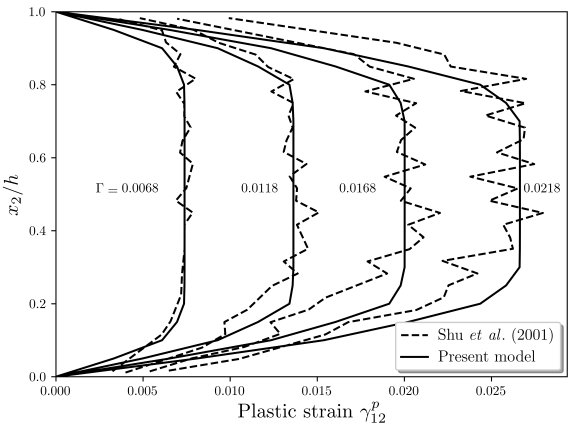

Fig. 10. Comparison between the plastic shear strain profiles obtained using the present model and those obtained by Shu et al. (2001) using discrete dislocation plasticity at different values of applied shear strain Γ under proportional loading conditions ($l_{en} = 0$, $l_{dis} = 0.3\,h$, $S_{\pi 0} = 15\,\text{MPa}$, $S_{\xi 0} = 3\,\text{MPa}$, $H_\pi = 0$, $H_\xi = 200\,\text{MPa}$).

dissipative stresses $\boldsymbol{\xi}^\alpha_{dis}$ at the onset of yield. It is worth recalling that, with the assumption of uncoupled dissipation, the higher-order dissipative stresses $\boldsymbol{\xi}^\alpha_{dis}$ depend only on plastic slip gradients and their rates, and then they continue to be zero after any uniform plastic straining. Therefore, the proposed model allows for avoiding elastic gaps not only at initial yield but also after any uniform plastic straining.

Concerning the non-proportional loading conditions, Fig. 11b presents the corresponding results obtained using different values of $S_{\xi 0}$, with $l_{dis} = h$ and $H_\xi = 100\,\text{MPa}$. This figure shows that, unlike l_{en}, the dissipative length scale l_{dis} can lead to elastic gaps not only at initial yield but also at the passivation of the top edge. For nonzero $S_{\xi 0}$, the gaps observed at initial yield under proportional loading conditions, with both edges passivated from the beginning, are divided into two parts. One part occurs at initial yield, where only the bottom edge is passivated; and the other part occurs at the passivation of the top edge. Under the considered non-proportional loading conditions, for zero (nearly zero) $S_{\xi 0}$, no apparent elastic gaps are observed, neither at initial yield nor at the occurrence of the non-proportional source. If the absence of elastic gaps at initial yield can be explained in the same way as beforehand, their absence at the passivation of the top edge is more difficult to explain. Indeed, with the bottom edge passivated from the beginning, nonuniform plastic strains develop within the studied strip before passivation of the top edge, making the current higher-order slip resistances S^α_ξ (and then $\boldsymbol{\xi}^\alpha_{dis}$) under evolution within the studied strip. To better explain the absence of elastic gaps in this case, the rate-sensitivity terms, which are only used for regularization, are ignored hereafter. In the rate-independent limit, avoidance of elastic gaps at the occurrence of a non-proportional loading source reveals the existence of nonzero plastic slip rates $\dot\gamma^\alpha$ that satisfy the microscopic balance equations (first line of system (20)). Assuming, for simplicity, that the boundary conditions are such that either $\dot\gamma^\alpha = 0$ or $\chi^\alpha = 0$ on the boundary, in the absence of higher-order energetic stresses, these equations can be written, in weak form, as:

$$G_\gamma = \sum_{\alpha=1}^{q} \int_{\mathcal{V}} \left[\left(|\tau^\alpha| - S^\alpha_\pi \right) \dot e^\alpha_\pi - S^\alpha_\xi \, \dot e^\alpha_\xi \right] dv = 0 \tag{79}$$

For this expression to have nonzero $\dot\gamma^\alpha$ solutions at the occurrence of a non-proportional loading source, the latter must not significantly alter the ratio between $\dot e^\alpha_\pi$ and $\dot e^\alpha_\xi$ in the regions where the higher-order dissipative stresses $\boldsymbol{\xi}^\alpha_{dis}$ are activated ($S^\alpha_\xi \neq 0$). Otherwise, the plastic flow is interrupted until the resolved shear stresses τ^α (evolving elastically) reach sufficient values to offset the disproportionate variations between terms of (79). By passivating only the bottom edge, plastic strain gradients develop only within the lower half of the

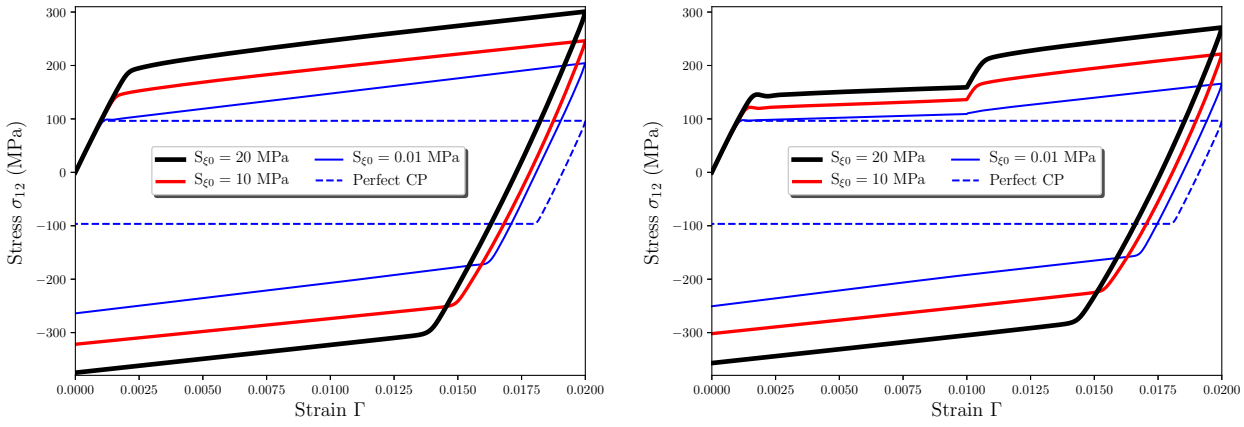

(a) Stress-strain curves under proportional loading

(b) Stress-strain curves under non-proportional loading

Fig. 11. Influence of the initial higher-order dissipative slip resistance $S_{\xi 0}$ on the elastic gap under proportional and non-proportional loading conditions ($l_{en} = 0$, $l_{dis} = h$, $H_\pi = 0$, $H_\xi = 100\,\mathrm{MPa}$).

studied strip (the plastic slip profiles are similar to those obtained at stage $4'$ in Fig. 4c). Using $S_{\xi 0} = 0$, after yielding, the stresses $\boldsymbol{\xi}^{\alpha}_{dis}$ are continuously activated (from $\mathbf{0}$) in this part of the strip and remain inactive otherwise. The occurrence of the top edge passivation modifies the plastic slip distributions only within the upper half of the studied strip, where the stresses $\boldsymbol{\xi}^{\alpha}_{dis}$ are not yet activated. This explains the absence of elastic gaps at the passivation of this edge.

By assuming uncoupled dissipation with $S_{\xi 0} = 0$, two important mechanisms generating or amplifying elastic gaps in conventional Gurtin-type models have been disabled. The first mechanism is due to the nonzero higher-order dissipative stresses $\boldsymbol{\xi}^{\alpha}_{dis}$ at their activation, and the second mechanism is due to the possible evolution of the current higher-order slip resistances S^{α}_{ξ} under uniform plastic straining. Disabling these mechanisms, the proposed model has allowed elastic gaps to be removed under the considered non-proportional loading conditions. However, this model is not completely gap-free in the sense that it cannot avoid gaps for any non-proportional loading conditions. Indeed, application of a loading source generating large variation in the plastic slip gradients within regions with activated higher-order dissipative stresses $\boldsymbol{\xi}^{\alpha}_{dis}$ can lead to elastic gaps. This would be the case if the studied strip is submitted to pure bending into the plastic range with microfree conditions followed by both edges passivation and continued bending (Fig. 12). In this case, the model can remove gaps only at initial yield. At the occurrence of the edges passivation, $S_{\xi 0}$ has only influence on the amplitude of the generated gaps but does not remove them. To the authors' knowledge, to date, there is no gap-free model in the literature including thermodynamically-consistent higher-order dissipative stresses, except for the very recent model of Panteghini et al. (2019) in which dissipation is implicitly embedded within the definition of the defect energy. It should be noted that the attitude taken here is rather agnostic on the occurrence of elastic gaps in reality. Some authors link these gaps to the size-dependence capabilities of gradient-based theories, whereas others see no physical reasons for their occurrence within a single crystal. Keeping with the latter opinion, Wulfinghoff et al. (2013) have proposed a SGCP approach with no elastic gaps (in effect, the involved higher-order stresses are assumed to be fully energetic and to stem from quadratic defect energy) for polycrystalline solids, in which the size-dependence effects are embedded within a grain boundary constitutive model. In the absence of experimental data for ruling on the existence of elastic gaps in reality, development of a model allowing for a more flexible control of these gaps, while explicitly including higher-order dissipative processes, would be very worthwhile.

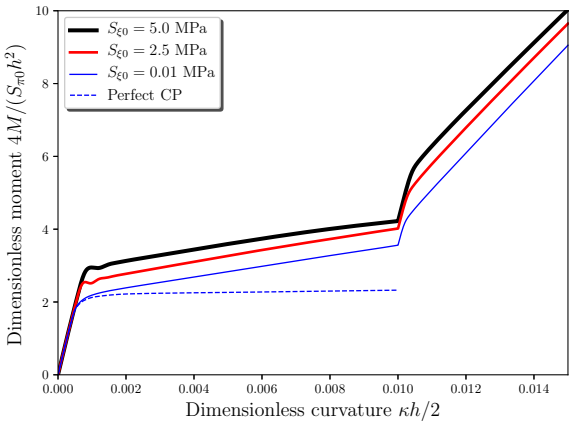

Fig. 12. Influence of the initial higher-order slip resistance $S_{\xi 0}$ on the moment-curvature response of the considered strip under pure bending with microfree conditions followed by top and bottom edges passivation and continued bending ($l_{en} = 0$, $l_{dis} = h$, $H_\pi = 0$, $H_\xi = 100\,\mathrm{MPa}$)

4.3. Interactions between microscopic stresses: recommendations for material parameters identification

Interaction between the different stresses involved in the SGCP model, including both first- and higher-order microscopic stresses, is presented in Fig. 13. Although only proportional loading conditions are applied for this figure, the following discussion is also valid for non-proportional loading conditions. At small scales, the global response of the considered material is (not surprisingly) more sensitive to the higher-order energetic and dissipative stresses. The energetic ones have mainly kinematic hardening effects, whereas the dissipative counterparts have isotropic hardening effects. The first-order dissipative stresses can also lead to isotropic hardening effects. However, compared to those generated by the higher-order ones, these effects have only small impact on the global material response. Using these observations, recommendations to identify the major model parameters for a real material are given hereafter. It is noteworthy, however, that, with the current understanding of dislocation physics, it is still early to confirm which small scale mechanisms must be considered in this model to correctly reproduce the small scale behavior of real materials. The great flexibility offered by the proposed model, thanks to the assumption of uncoupled dissipation, in controlling a wide selection of these mechanisms makes the task of switching between them relatively easy.

Using the dissipation uncoupling assumption, the constitutive equations of the first-order dissipative stresses correspond exactly to those classically used to describe the evolution of the resolved shear stresses in the context of conventional crystal plasticity. It is then suggested to separately identify the parameters of these equations in such a way as to reproduce the behavior of the considered material in the absence of size effects. This allows for application of the model on large specimens in which size effects are negligible. To this end, experimental results obtained using relatively large samples with sufficient number of grains must be used for the identification of these parameters. Note that such parameters can also be found in literature for several common materials. To model size effects at small scales, the higher-order constitutive parameters must then be included and identified. Preliminary experimental tests under cyclic loading would be necessary to determine which higher-order parameters are required. If only kinematic hardening is obtained, parameters associated with higher-order dissipative stresses can be neglected ($l_{dis} = 0$). On the contrary, if mainly isotropic hardening is found, parameters associated with higher-order energetic stresses may be ignored ($l_{en} = 0$). If combined hardening is obtained, all higher-order parameters need to be taken into consideration. The retained parameters can finally be identified based on further experimental tests implying small specimens with different grain sizes to find out about the elastic gaps. In the case of higher-order energetic stresses, these gaps can be controlled by $n < 2$ and l_{en}. Although not treated in this work, the

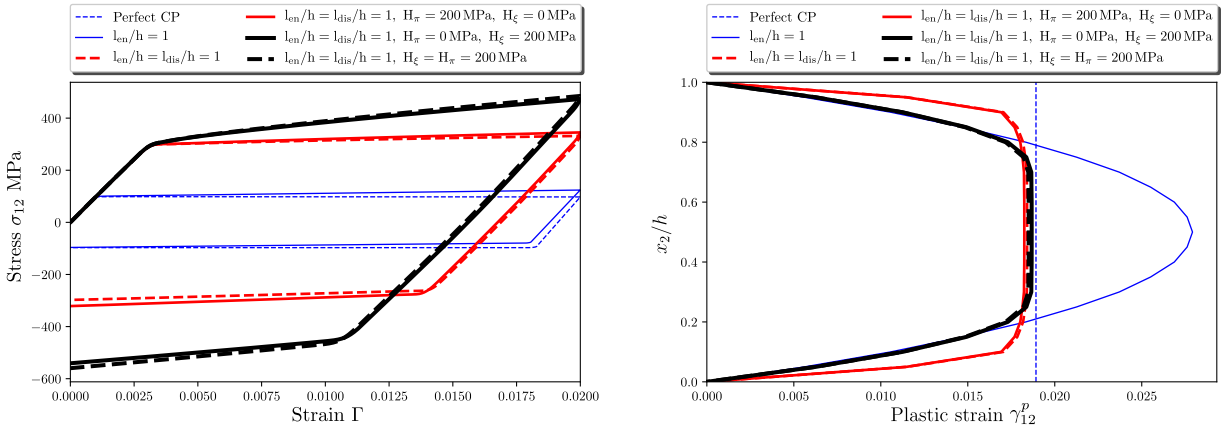

(a) Stress-strain curves

(b) Plastic shear strain distributions along $\mathbf{e}_2$ direction

Fig. 13. Interaction between the different stresses involved in the proposed SGCP model under proportional loading ($n = 2$, $S_{\xi 0} = 50\,\mathrm{MPa}$).

higher-order energetic slip resistance X_0 can also influence such gaps in the range of $n < 2$. According to expressions of higher-order energetic stresses, this parameter behaves as l_{en}^n and may be used to control the range in which l_{en} contributes to material hardening and/or strengthening. In the case of higher-order dissipative stresses, the elastic gaps can be controlled by $S_{\xi 0}$ and l_{dis}. Depending on the number of retained constitutive parameters to be identified, robust identification algorithms can be applied to simplify this task (Chtourou et al., 2017). It should, however, be noted that these algorithms are generally based on mathematical optimization and do not necessarily lead to a unique set of optimized parameters.

5. Conclusion

A flexible Gurtin-type strain gradient crystal plasticity (SGCP) model has been developed in this paper, based on non-quadratic defect energy and uncoupled dissipation. Both energetic (recoverable) and dissipative (unrecoverable) microscopic stresses are considered in this model. The higher-order energetic microscopic stresses are derived from a generalized power-law defect energy, with adjustable order-controlling index n. This form of defect energy is proposed to investigate the interaction between the form of this energy and the energetic length scale effects under proportional and non-proportional loading conditions. In spirit of multi-criterion approaches available in the literature (Forest et al., 1997, 2000; Forest and Sievert, 2003; Fleck et al., 2014; Panteghini et al., 2019), the dissipative microscopic stresses are derived from an uncoupled dissipation functional, which is expressed as a sum of two separate functions of first- and higher-order effective plastic strain measures. To evaluate the proposed SGCP model and to investigate the influence of its major constitutive parameters, a simplified two-dimensional (2D) version of this model was derived and implemented within the commercial finite element package Abaqus/Standard, using a User-ELment (UEL) subroutine. This version was then applied to simulate the classical 2D simple shear problem of a constrained crystalline strip submitted to proportional and non-proportional loading conditions. Major simulation results and conclusions are recalled hereafter.

Starting with the energetic length scale effects, it was found that these effects depend on the value of the order-controlling index n and loading conditions. Two cases can be distinguished: $n < 2$ and $n \geq 2$. In the range of $n < 2$, the energetic length scale l_{en} leads to unusual nonlinear kinematic hardening, resulting in an apparent increase of the yield strength (strengthening) under monotonic loading. This is in accordance with results from the literature (*e.g.,* Fleck and Willis, 2015; Wulfinghoff et al., 2015; El-Naaman et al., 2019).

Under non-proportional loading conditions, more complex kinematic hardening with additional inflection points is obtained. Interestingly, these additional points take place at approximately the same plastic state at which the non-proportional loading source occurred, revealing new loading history memory-like effects of l_{en}. The unusual nonlinear kinematic hardening with inflection points, at least that obtained under proportional loading conditions, complies with the kinematic hardening type III (KIII) of Asaro (1975). It corresponds to a "first in/last out" sequence of dislocation motion and represents the most perfect form of recovery of plastic memory. Although uncommon, this phenomenon has already been observed experimentally in some polycrystalline materials, such as Fe-Cr alloys (Taillard and Pineau, 1982). For $n < 2$, KIII type hardening is the only active hardening mechanism, allowing for accurate continuum description of the piling-up and unpiling-up phenomena. Increasing n (*i.e.*, n approaching 2), this hardening type becomes less and less marked and vanishes at $n = 2$ to be replaced by the classical kinematic hardening (KI type hardening, in the terminology of Asaro (1975)). From $n = 2$, regardless of loading type, l_{en} has only influence on the rate of hardening after yielding but not on the material strengthening, as widely recognized in the literature.

Concerning dissipation aspects, in terms of stress-strain response, the assumption of uncoupled dissipation has no significant impact. It leads to a slight overestimation of the yield strength, compared to the results of Gurtin et al. (2007), which are obtained using coupled dissipation. This overestimation is due to the fact that the uncoupled plastic strain measures used in the present model predict slightly smaller values, compared to those which can be obtained using coupled measures (Gurtin et al., 2007). This results in overestimating the dissipative microscopic stresses and then the energetic macroscopic stress $\boldsymbol{\sigma}$ via the flow rule (59). However, in terms of plastic shear strain distributions across the thickness of the studied strip, quite different results were obtained depending on whether coupled or uncoupled dissipation is adopted. Using the assumption of uncoupled dissipation, obvious boundary layers develop in the vicinity of the top and bottom edges of the studied strip. Beyond these layers, the plastic shear strain becomes near-uniform with a plateau-shaped distribution. On the contrary, using coupled dissipation, the plastic shear strain distributions obtained by Gurtin et al. (2007) have always near-quadratic forms, even outside the boundary layers. The distributions of plastic shear strain obtained in this work, with obvious boundary layers and a plateau outside the layers, seem to be more in accordance with those produced by discrete dislocation simulations in the work of Shu et al. (2001) and Bittencourt et al. (2003). Accurately capturing boundary layer effects is essential since they represent important nonlocal (size) effects that emerge at small scales. The thickness of these layers can easily be controlled by the higher-order hardening modulus H_{ξ}. Another advantage of using uncoupled dissipation is the flexible control of some important dissipative effects, such as elastic gaps, which can easily be controlled by varying the initial higher-order slip resistance $S_{\xi 0}$. By canceling the latter parameter, a variant of the proposed model can be obtained that allows for removing such gaps under certain circumstances, e.g. at initial yield or, in a general manner, when a non-proportional loading source does not significantly variate the plastic slip gradients within regions in which the higher-order dissipative stresses are activated.

Although it is still early to confirm which small scale mechanisms must be considered to correctly reproduce the small scale behavior of real materials, the proposed model, with its energetic and dissipative parts, offers a great flexibility in monitoring major of these mechanisms. This makes the task of switching between them relatively easy.

Acknowledgment

The authors are grateful to Samuel Forest for valuable discussions regarding physical and numerical aspects of strain gradient crystal plasticity and for helpful comments on the nonlinear kinematic hardening effects of the energetic length scale. They are also indebted to Lorenzo Bardella for insightful discussions

resulting in improving the manuscript. The author Lei CAI acknowledges the financial support of China Scholarship Council (CSC201706280201).

References

Acharya, A., Bassani, J. L., 2000. Lattice incompatibility and a gradient theory of crystal plasticity. J. Mech. Phys. Solids 48 (8), 1565–1595.

Aifantis, E. C., 1984. On the microstructural origin of certain inelastic models. J. Eng. Mater. Technol. 106 (4), 326.

Anand, L., Aslan, O., Chester, S. A., 2012. A large-deformation gradient theory for elastic-plastic materials: Strain softening and regularization of shear bands. Int. J. Plast. 30-31, 116–143.

Anand, L., Gurtin, M. E., Reddy, B. D., 2015. The stored energy of cold work, thermal annealing, and other thermodynamic issues in single crystal plasticity at small length scales. Int. J. Plast. 64, 1–25.

Arsenlis, A., Parks, D. M., 1999. Crystallographic aspects of geometrically-necessary and statistically-stored dislocation density. Acta Mater. 47 (5), 1597–1611.

Asaro, R. J., 1975. Elastic-plastic memory and kinematic-type hardening. Acta Metall. 23 (10), 1255–1265.

Ashby, M. F., 1970. The deformation of plastically non-homogeneous materials. Philos. Mag. 21 (170), 399–424.

Bardella, L., 2010. Size effects in phenomenological strain gradient plasticity constitutively involving the plastic spin. Int. J. Eng. Sci. 48 (5), 550–568.

Bardella, L., Panteghini, A., 2015. Modelling the torsion of thin metal wires by distortion gradient plasticity. J. Mech. Phys. Solids 78, 467–492.

Bilby, B. A., Bullough, R., Smith, E., 1955. Continuous distributions of dislocations: a new application of the methods of non-riemannian geometry. Proc. R. Soc. Lond. A 231 (1185), 263–273.

Bittencourt, E., 2018. On the effects of hardening models and lattice rotations in strain gradient crystal plasticity simulations. Int. J. Plast. 108, 169–185.

Bittencourt, E., Needleman, A., Gurtin, M. E., Van der Giessen, E., 2003. A comparison of nonlocal continuum and discrete dislocation plasticity predictions. J. Mech. Phys. Solids 51 (2), 281–310.

Chtourou, R., Leconte, N., Zouari, B., Chaari, F., Markiewicz, E., Langrand, B., 2017. Macro-modeling of spot weld strength and failure: Formulation and identification procedure based on pure and mixed modes of loading. Eng. Computation 34 (3), 941–959.

Clayton, J. D., Bammann, D. J., McDowell, D. L., 2005. A geometric framework for the kinematics of crystals with defects. Philos. Mag. 85 (33-35), 3983–4010.

Cordero, N. M., Gaubert, A., Forest, S., Busso, E. P., Gallerneau, F., Kruch, S., 2010. Size effects in generalised continuum crystal plasticity for two-phase laminates. J. Mech. Phys. Solids 58 (11), 1963–1994.

Dahlberg, C. F. O., Boåsen, M., 2019. Evolution of the length scale in strain gradient plasticity. Int. J. Plast. 112, 220–241.

Dahlberg, C. F. O., Faleskog, J., 2014. Strain gradient plasticity analysis of the influence of grain size and distribution on the yield strength in polycrystals. Eur. J. Mech. - A/Solids 44, 1–16.

Dahlberg, C. F. O., Saito, Y., Öztop, M. S., Kysar, J. W., 2017. Geometrically necessary dislocation density measurements at a grain boundary due to wedge indentation into an aluminum bicrystal. J. Mech. Phys. Solids 105, 131–149.

El-Naaman, S. A., Nielsen, K. L., Niordson, C. F., 2016. On modeling micro-structural evolution using a higher order strain gradient continuum theory. International Journal of Plasticity 76, 285–298.

El-Naaman, S. A., Nielsen, K. L., Niordson, C. F., 2019. An investigation of back stress formulations under cyclic loading. Mechanics of Materials 130, 76–87.

Fleck, N. A., Hutchinson, J. W., 2001. A reformulation of strain gradient plasticity. J. Mech. Phys. Solids 49 (10), 2245–2271.

Fleck, N. A., Hutchinson, J. W., Willis, J. R., 2014. Strain gradient plasticity under non-proportional loading. Proc. R. Soc. A Math. Phys. Eng. Sci. 470 (2170), 0267.

Fleck, N. A., Hutchinson, J. W., Willis, J. R., 2015. Guidelines for constructing strain gradient plasticity theories. J. Appl. Mech. 82 (7), 071002.

Fleck, N. A., Willis, J. R., 2015. Strain gradient plasticity: energetic or dissipative? Acta Mech. Sin. 31 (4), 465–472.

Forest, S., Barbe, F., Cailletaud, G., 2000. Cosserat modelling of size effects in the mechanical behaviour of polycrystals and multi-phase materials. Int. J. Solids Struct. 37, 7105–7126.

Forest, S., Cailletaud, G., Sievert, R., 1997. A cosserat theory for elastoviscoplastic single crystals at finite deformation. Arch. Mech. 49 (4), 705–736.

Forest, S., Guéninchault, N., 2013. Inspection of free energy functions in gradient crystal plasticity. Acta Mech. Sin. Xuebao 29 (6), 763–772.

Forest, S., Mayeur, J. R., McDowell, D. L., 2019. Micromorphic crystal plasticity. In: Handb. Nonlocal Contin. Mech. Mater. Struct. Springer International Publishing, Cham, pp. 643–686.

Forest, S., Sievert, R., 2003. Elastoviscoplastic constitutive frameworks for generalized continua. Acta Mech. 160 (1-2), 71–111.

Groma, I., Csikor, F. F., Zaiser, M., 2003. Spatial correlations and higher-order gradient terms in a continuum description of dislocation dynamics. Acta Mater. 51 (5), 1271–1281.

Gudmundson, P., 2004. A unified treatment of strain gradient plasticity. J. Mech. Phys. Solids 52 (6), 1379–1406.

Gurtin, M. E., 2002. A gradient theory of single-crystal viscoplasticity that accounts for geometrically necessary dislocations. J. Mech. Phys. Solids 50 (1), 5–32.

Gurtin, M. E., 2004. A gradient theory of small-deformation isotropic plasticity that accounts for the Burgers vector and for dissipation due to plastic spin. J. Mech. Phys. Solids 52 (11), 2545–2568.

Gurtin, M. E., 2008. A finite-deformation, gradient theory of single-crystal plasticity with free energy dependent on densities of geometrically necessary dislocations. Int. J. Plast. 24 (4), 702–725.

Gurtin, M. E., 2010. A finite-deformation, gradient theory of single-crystal plasticity with free energy dependent on the accumulation of geometrically necessary dislocations. Int. J. Plast. 26 (8), 1073–1096.

Gurtin, M. E., Anand, L., 2009. Thermodynamics applied to gradient theories involving the accumulated plastic strain: The theories of Aifantis and Fleck and Hutchinson and their generalization. J. Mech. Phys. Solids 57 (3), 405–421.

Gurtin, M. E., Anand, L., Lele, S. P., 2007. Gradient single-crystal plasticity with free energy dependent on dislocation densities. J. Mech. Phys. Solids 55 (9), 1853–1878.

Hayashi, I., Sato, M., Kuroda, M., 2011. Strain hardening in bent copper foils. J. Mech. Phys. Solids 59 (9), 1731–1751.

Hurtado, D. E., Ortiz, M., 2013. Finite element analysis of geometrically necessary dislocations in crystal plasticity. Int. J. Numer. Methods Eng. 93 (1), 66–79.

Hutchinson, J. W., 2012. Generalizing J 2 flow theory: Fundamental issues in strain gradient plasticity. Acta Mech. Sin. 28 (4), 1078–1086.

Jiang, M., Devincre, B., Monnet, G., 2019. Effects of the grain size and shape on the flow stress: A dislocation dynamics study. Int. J. Plast. 113, 111–124.

Kalidindi, S. R., Bronkhorst, C. A., Anand, L., 1992. Crystallographic texture evolution in bulk deformation processing of FCC metals. J. Mech. Phys. Solids 40 (3), 537–569.

Klusemann, B., Svendsen, B., Vehoff, H., 2013. Modeling and simulation of deformation behavior, orientation gradient development and heterogeneous hardening in thin sheets with coarse texture. Int. J. Plast. 50, 109–126.

Klusemann, B., Yalçinkaya, T., 2013. Plastic deformation induced microstructure evolution through gradient enhanced crystal plasticity based on a non-convex Helmholtz energy. Int. J. Plast. 48, 168–188.

Kondo, K., 1964. On the analytical and physical foundations of the theory of dislocations and yielding by the differential geometry of continua. Int. J. Eng. Sci. 2 (3), 219–251.

Kröner, E., 1958. Kontinuumstheorie der versetzungen und eigenspannungen. Vol. 5. Springer.

Lardner, R. W., 1969. Dislocation dynamics and the theory of the plasticity of single crystals. Z. Angew. Math. Phys. 20 (4), 514–529.

Le, K. C., Stumpf, H., 1996. Nonlinear continuum theory of dislocations. Int. J. Engng. Sci. 34 (3), 339–358.

Ling, C., Forest, S., Besson, J., Tanguy, B., Latourte, F., 2018. A reduced micromorphic single crystal plasticity model at finite deformations. Application to strain localization and void growth in ductile metals. Int. J. Solids Struct. 134, 43–69.

Liu, D., He, Y., Dunstan, D. J., Zhang, B., Gan, Z., Hu, P., Ding, H., 2013. Toward a further understanding of size effects in the torsion of thin metal wires: An experimental and theoretical assessment. Int. J. Plast. 41, 30–52.

Ma, Z. S., Zhou, Y. C., Long, S. G., Lu, C., 2012. On the intrinsic hardness of a metallic film/substrate system: Indentation size and substrate effects. Int. J. Plast. 34, 1–11.

Mayeur, J. R., McDowell, D. L., 2014. A comparison of Gurtin type and micropolar theories of generalized single crystal plasticity. Int. J. Plast. 57, 29–51.

Mayeur, J. R., McDowell, D. L., Bammann, D. J., 2011. Dislocation-based micropolar single crystal plasticity: Comparison of multi- and single criterion theories. J. Mech. Phys. Solids 59 (2), 398–422.

Mühlhaus, H. B., Alfantis, E. C., 1991. A variational principle for gradient plasticity. Int. J. Solids Struct. 28 (7), 845–857.

Nellemann, C., Niordson, C. F., Nielsen, K. L., 2017. An incremental flow theory for crystal plasticity incorporating strain gradient effects. Int. J. Solids Struct. 110-111, 239–250.

Nellemann, C., Niordson, C. F., Nielsen, K. L., 2018. Hardening and strengthening behavior in rate-independent strain gradient crystal plasticity. Eur. J. Mech. A/Solids, 157–168.

Niordson, C. F., Hutchinson, J. W., 2003. On lower order strain gradient plasticity theories. Eur. J. Mech. A/Solids 22 (6), 771–778.

Nye, J. F., 1953. Some geometrical relations in dislocated crystals. Acta Metall. 1 (2), 153–162.

Ohno, N., Okumura, D., 2007. Higher-order stress and grain size effects due to self-energy of geometrically necessary dislocations. J. Mech. Phys. Solids 55 (9), 1879–1898.

Ohno, N., Okumura, D., Shibata, T., 2009. Grain-size dependent yield behavior under loading, unloading and reverse loading. Int. J. Mod. Phys. B 22 (31n32), 5937–5942.

Panteghini, A., Bardella, L., 2016. On the Finite Element implementation of higher-order gradient plasticity, with focus on theories based on plastic distortion incompatibility. Comput. Methods Appl. Mech. Eng. 310, 840–865.

Panteghini, A., Bardella, L., Niordson, C. F., 2019. A potential for higher-order phenomenological strain gradient plasticity to predict reliable response under non-proportional loading. Proc. R. Soc. A.

Petryk, H., Stupkiewicz, S., 2016. A minimal gradient-enhancement of the classical continuum theory of crystal plasticity. part i: The hardening law. Arch. Mech. 68 (6), 459–485.

Polizzotto, C., 2010. Strain gradient plasticity, strengthening effects and plastic limit analysis. Int. J. Solids Struct. 47 (1), 100–112.

Polizzotto, C., 2014. Surface effects, boundary conditions and evolution laws within second strain gradient plasticity. Int. J. Plast. 60, 197–216.

Ryś, M., Petryk, H., 2018. Gradient crystal plasticity models with a natural length scale in the hardening law. Int. J. Plast. 111, 168–187.

Sarac, A., Oztop, M. S., Dahlberg, C. F. O., Kysar, J. W., 2016. Spatial distribution of the net burgers vector density in a deformed single crystal. Int. J. Plast. 85, 110–129.

Shu, J. Y., Fleck, N. A., Van der Giessen, E., Needleman, A., 2001. Boundary layers in constrained plastic flow: comparison of nonlocal and discrete dislocation plasticity. J. Mech. Phys. Solids 49 (6), 1361–1395.

Stoltz, R. E., Pelloux, R. M., 1976. The bauschinger effect in precipitation strengthened aluminum alloys. Metall. Trans. A 7 (8), 1295–1306.

Stupkiewicz, S., Petryk, H., 2016. A minimal gradient-enhancement of the classical continuum theory of crystal plasticity. part ii: Size effects. Arch. Mech. 68 (6), 487–513.

Taillard, R., Pineau, A., 1982. Room temperature tensile properties of Fe-19wt.%Cr alloys precipitation hardened by the intermetallic compound NiAl. Mater. Sci. Eng. 56 (3), 219–231.

Teodosiu, C., Sidoroff, F., 1976. A theory of finite elastoviscoplasticity of single crystals. Int. J. Eng. Sci. 14, 713–723.

Voyiadjis, G. Z., Song, Y., 2019. Strain gradient continuum plasticity theories: Theoretical, numerical and experimental investigations. Int. J. Plast.

Wulfinghoff, S., Bayerschen, E., Böhlke, T., 2013. A gradient plasticity grain boundary yield theory. Int. J. Plast. 51, 33–46.

Wulfinghoff, S., Böhlke, T., 2015. Gradient crystal plasticity including dislocation-based work-hardening and dislocation transport. Int. J. Plast. 69, 152–169.

Wulfinghoff, S., Forest, S., Böhlke, T., 2015. Strain gradient plasticity modeling of the cyclic behavior of laminate microstructures. J. Mech. Phys. Solids 79, 1–20.

Yalçinkaya, T., Brekelmans, W. A. M., Geers, M. G. D., 2011. Deformation patterning driven by rate dependent non-convex strain gradient plasticity. J. Mech. Phys. Solids 59 (1), 1–17.

Zhou, C., Lesar, R., 2012. Dislocation dynamics simulations of plasticity in polycrystalline thin films. Int. J. Plast. 30-31, 185–201.